

# SPACE-TIME SPECTRAL ELEMENT METHOD FOR TOPOLOGY OPTIMIZATION OF TRANSIENT HEAT CONDUCTION\*

SARAH NATAJ<sup>†</sup>, MAGNUS APPEL<sup>†</sup>, AND JOE ALEXANDERSEN<sup>‡</sup>

**Abstract.** We develop a space–time spectral element method for topology optimization of transient heat conduction. The forward problem is discretized with summation–by–parts (SBP) operators, and interface/boundary and initial/terminal conditions are imposed weakly via simultaneous approximation terms (SAT), yielding a stable monolithic space–time scheme on heterogeneous domains. Stability is proven under specific conditions on the SAT parameters, scaled with the spatial mesh resolution and material properties. We compute design sensitivities using a discrete space–time adjoint scheme that is dual-consistent with the primal SBP–SAT scheme. Dual consistency ensures that the discrete adjoint consistently approximates the continuous dual problem and, under standard smoothness assumption, yields superconvergent functional estimates. We validate the resulting optimal designs by comparison with independently computed reference optimal design and report time-to-solution and cost-of-accuracy curves, comparing against low-order time-marching and all-at-once solvers for the forward and adjoint systems. The proposed scheme attains high accuracy with fewer space–time degrees of freedom and remains stable, reducing time-to-solution and memory compared with an alternative all-at-once solver. This makes it a future candidate for large-scale topology optimization of time-dependent thermal systems.

**Key words.** space-time methods, topology optimization, transient conduction, spectral element, summation-by-parts, simultaneous-approximation-terms

**MSC codes.** 65M70, 65M12, 49M41, 74P15, 65K10, 80A19, 80M22, 80M50,

**1. Introduction.** Topology optimization is a computational design methodology for finding an optimal material distribution within a given domain that minimizes a given objective functional subject to governing physics and design constraints [1, 2]. Beyond classical structural applications in solid mechanics, modern uses span electromagnetic, thermal, acoustic, and fluid dynamics problems; see the survey articles [3, 4]. Here we focus on transient heat conduction and optimize material layouts to steer the temperature field over time. This problem has been widely studied in the literature [5, 6, 7, 8, 9].

We adopt an adjoint-based sensitivity framework for the partial differential equation (PDE) constrained optimization problem. Design sensitivities are computed via a discrete adjoint and require one forward and one backward solve. Unlike a topology optimization problem for steady-state PDEs, where only one state needs to be computed and stored for adjoint sensitivity analysis, an optimization problem subject to time-dependent PDEs must consider an entire time history [10, 11]. Therefore, the adjoint method for unsteady problems typically requires storing the state at all time steps. This, plus the necessity to perform many optimization iterations, makes time-dependent topology optimization extremely computationally demanding. Another fundamental challenge is the sequential nature of time integration. Conventional approaches march forward in time step by step for the state, then backward in time for the adjoint. This limits parallelism, even if the spatial domain is parallelized among processors, as computations must be performed sequentially in time.

---

\*Submitted to *SIAM Journal on Scientific Computing (SISC)*, Nov 2025 .

**Funding:** The work has been funded by Independent Research Foundation Denmark (DFF) through a Sapere Aude Research Leader grant (3123-00020B) for the COMFORT project (COmputational Morphogenesis FOR Time-dependent problems).

<sup>†</sup>Institute of Mechanical and Electrical Engineering, University of Southern Denmark, (rena@sdu.dk, magap@sdu.dk, joal@sdu.dk).

Space–time methods provide a powerful approach to address these challenges. In a space–time formulation, the time dimension is treated similarly to a spatial dimension, enabling a fully simultaneous solution over all time steps. This approach eliminates the sequential time-stepping bottleneck by solving all time steps in a single unified system, preferably by parallelizing across time. The trade-off is that the associated linear system is significantly larger and often ill-conditioned. Efficient parallel solvers and preconditioners are required to handle the resulting very large linear systems. Recent literature has begun to explore strategies in topology optimization to reduce runtime [12, 13] and memory usage [12, 14, 15] for transient problems.

Much of the work in this direction, however, employs low-order spatial and temporal schemes. Theulings et al. [12] use a finite-volume discretization on Cartesian grids with an explicit forward Euler scheme in time for solving a heat conduction problem and implicit backward Euler scheme for solving a fluid dynamics problem. Appel and Alexandersen’s one-shot Parareal study [13] adopts a Galerkin finite-element discretization with bilinear spatial shape functions and first-order backward Euler scheme in time. Their space–time multigrid paper [16] targets an all-at-once BE–FE formulation (linear finite element in space, backward Euler in time) on uniform space–time meshes. In [17] they use a continuous Galerkin space–time finite element method with linear elements in both space and time, with an added artificial diffusion in the time direction for stability, achieving a first-order accuracy in time. Overall, these studies emphasize solver efficiency and parallelism while retaining low-order discretizations. Low-order spatial elements are common in topology optimization, since the design freedom is coupled to the mesh resolution (usually one design variable per element) and thus requires many spatial elements. Low-order elements allows to keep total computational cost relatively low when needing fine meshes for high design freedom. However, this does not need to translate to temporal schemes, where usually the design will remain constant over time. Thus, we explore high-order temporal discretization herein.

High-order discretization of time-dependent PDEs, in both space and time offers improved solution accuracy and convergence rates with fewer space–time degrees of freedom (DoFs) in comparison to standard low-order finite elements and finite difference methods. Adjoint methods compatible with high-order discretizations for unsteady flow optimization have been established in the literature [18, 19], providing a methodological basis for topology optimization studies employing spectral element, Fourier spectral, or discontinuous Galerkin-type discretizations [20, 21, 22].

Schemes built from high-order differentiation operators that satisfy the summation-by-parts (SBP) property [23, 24] provide a principled path to stability in the fully discrete setting. Coupled with simultaneous approximation terms (SAT) [25, 26], they weakly enforce boundary and interface conditions while replicating integration-by-parts at the discrete level. The resulting SBP–SAT formulations admit discrete energy estimates that mirror their continuous problems and thereby prevent the spurious growth of numerical energy. The SBP–SAT approach has previously been used successfully to construct provably stable high-order discretizations of the conjugate heat transfer (CHT) problem using a semi-discrete approach [27, 28, 29].

Building on SBP–in–time developments [30, 31, 32] and dual consistent SBP schemes [33, 34], we construct a space–time spectral element SBP–SAT method for both primal and adjoint problems. Due to the SBP property of the differentiation operator together with compatibly constructed space/time boundary and interface SATs, the algebraic adjoint of the discrete state operator coincides with a consistent discretization of the continuous adjoint (discrete dual consistency). Dual (adjoint)

consistency is a key property of a discretization and is typically required to obtain optimal-order convergence for given functionals [35, 36]. In particular, a linear functional is called superconvergent if the error in its discrete approximation converges at a higher order than the underlying solution error [37, 38]. It is known that dual consistent SBP finite-difference discretizations, when paired with an energy-stable discretization, yield superconvergent linear functionals under standard regularity conditions [39, 40]. By analogy, our proposed space-time spectral-element SBP-SAT scheme is designed to satisfy the same conditions, and we observe superconvergent functional errors in practice. To our knowledge, this extension to space-time spectral elements is new.

The main contributions of this article are as follows. We develop a space-time spectral element scheme based on SBP-SAT operators. The framework provides flexibility in the choice of discretization: spectral element (SE) can be replaced by finite-difference (FD), finite-volume (FV), discontinuous-Galerkin (DG), or continuous-Galerkin (CG) discretizations that admit the SBP properties. We enforce the initial, boundary and interface conditions weakly using SATs and prove stability under suitable choices of the SAT parameters, scaled with the spatial mesh resolution and material properties. We employ a space-time adjoint scheme that is discrete dual-consistent with the SBP-SAT primal scheme, so the discrete adjoint scheme is a consistent discretization of the continuous dual problem and yields superconvergent functional estimates under standard smoothness conditions.

The paper is organized as follows. Section 2 states the model and optimization problem, introduces the space-time spectral element SBP-SAT discretization, and derives the discrete adjoint and sensitivities formulae. Section 3 presents numerical experiments that validate the optimal designs by comparison with independently computed reference designs and assess accuracy and efficiency of the proposed scheme. Section 4 gives a conclusion.

**2. Methodology.** For simplicity, this work considers transient heat conduction in one spatial dimension. Let  $a < b$  be given and let  $T > 0$  denote the terminal time, and define the space-time domain  $\Omega := (a, b) \times (0, T)$ . Let  $u(x, t)$  denote the temperature field and  $f(x, t)$  the external heat load per unit volume.

The presence of conductive or insulating material is parameterized by a function,  $\rho(x)$ , which is referred to as the “design field” and as “design variables” after discretization. Inside the insulator,  $\rho(x) = 0$ , and inside the conductor,  $\rho(x) = 1$ . In density-based topology optimization,  $\rho$  is relaxed to vary continuously between 0 and 1, and penalization is employed to drive the solution toward the discrete values 0 and 1 [2]. An overview of alternative methods is given by Sigmund and Maute [41].

The thermal diffusivity  $\kappa$  depends on the material distribution and is given by

$$(2.1) \quad \kappa(\rho(x)) = \kappa_{\min} + (\kappa_{\max} - \kappa_{\min}) \rho(x)^p.$$

where  $\kappa_{\min}$ ,  $\kappa_{\max}$ , and  $p \geq 1$  are known positive constants. We consider a non-dimensionalized model, therefore thermal diffusivity  $\kappa$  denotes the  $k/\rho_m c_p$ , where  $k$  is the thermal conductivity,  $\rho_m$  is the mass density, and  $c_p$  is the mass-specific heat capacity at constant pressure.

The optimization problem is then formulated as a minimization of the squared temperature integrated over time and space to ensure rapid heat dissipation throughout the interval, subject to a material volume bound  $V^*$ . In contrast to the thermal compliance objective, which emphasizes regions where heat is applied, the chosen objective functional penalizes elevated temperature everywhere, yielding designs that

improve global cooling performance.

Our continuous topology optimization problem is formulated as

$$\begin{aligned}
 \min_{u, \rho} \quad & J(u, \rho) = \int_0^T \int_a^b u(x, t)^2 dx dt, \\
 \text{s.t. :} \quad & \frac{\partial u}{\partial t}(x, t) = \frac{\partial}{\partial x} \left( \kappa(\rho(x)) \frac{\partial u}{\partial x}(x, t) \right) + f(x, t), \quad (x, t) \in \Omega, \\
 (2.2) \quad & u(a, t) = h(t), \quad u(b, t) = g(t), \quad t \in [0, T], \\
 & u(x, 0) = q(x), \quad x \in [a, b], \\
 & \int_a^b \rho(x) dx \leq V^*, \quad 0 \leq \rho(x) \leq 1,
 \end{aligned}$$

where  $V^*$  is the prescribed material volume bound over the whole spatial domain. We adopt a discretize-then-optimize strategy [42] the PDE and the objective are first discretized in space-time where we employ SBP differentiation operators to discretize spatial and temporal derivatives and apply SATs to impose initial, and interface conditions in a stable monolithic manner [43]. a discretize-then-optimize strategy [42] the PDE and the objective are first discretized in space-time where we employ SBP differentiation operators to discretize spatial and temporal derivatives and apply SATs to impose initial, boundary and interface conditions in a stable monolithic manner [43].

We assume the domain  $\Omega$  is partitioned into  $K$  design cells  $\{\Omega_k\}_{k=1}^K$  and  $\rho \in [0, 1]^K$  denotes the design vector. Let  $\mathbf{u} \in \mathbb{R}^N$  denote the vector of stacked temperature unknowns at all  $N$  space-time nodes. The discrete objective is the space-time integrated squared temperature  $J(\mathbf{u}, \rho) = \mathbf{u}^\top \mathbf{P} \mathbf{u}$ , where the weight matrix  $\mathbf{P}$  is a symmetric positive definite matrix. The state  $\mathbf{u}$  and the design  $\rho$  are related by the discrete residual  $\mathcal{R}(\mathbf{u}, \rho) = \mathbf{0}$ , assembled from the space-time SBP-SAT scheme described in Section 2.1. Instead of treating the discrete residual explicitly as a constraint, we follow the nested approach [2] where the discrete residual is solved at each design iteration. The discrete form of the topology optimization problem is then given by

$$\begin{aligned}
 \min_{\rho} \quad & J(\mathbf{u}, \rho) = \mathbf{u}^\top \mathbf{P} \mathbf{u} \quad \text{where } \mathbf{u} \text{ satisfies } \mathcal{R}(\mathbf{u}, \rho) = \mathbf{0}, \\
 (2.3) \quad \text{s.t.} \quad & \sum_{k=1}^K \rho^{(k)} V^{(k)} \leq V^*,
 \end{aligned}$$

where  $V^{(k)} = |\Omega_k|$ .

At each iteration, we first solve the forward problem  $\mathcal{R}(\mathbf{u}, \rho) = \mathbf{0}$  for  $\mathbf{u}$  with the current design  $\rho$ ; followed by solving the adjoint equation for adjoint vector variable  $\Lambda$ ,

$$\left( \frac{\partial \mathcal{R}}{\partial \mathbf{u}} \right)^\top \Lambda = \frac{\partial J}{\partial \mathbf{u}}.$$

Then we compute the design sensitivity

$$\nabla_\rho J = -\Lambda^\top \frac{\partial \mathcal{R}}{\partial \rho}.$$

Finally, we update the design  $\rho$  using the method of moving asymptotes (MMA) [44], subject to the volume constraint. MMA is a widely adopted method for large-scale density-based topology optimization with one or more constraints. It solves convex separable approximated subproblems of the nonlinear/nonconvex problem using

adaptive bounds to efficiently update the design. For brevity, we omit algorithmic details and refer the reader to [44] for the method and its application to topology optimization. Each iteration requires one forward and one adjoint solve, followed by computation of the sensitivity in all space–time elements. These steps are repeated until the desired convergence is achieved.

In the following, we detail these steps: Section 2.1 reviews the basics of SBP operators and the assembly of the discrete residual using a stable, monolithic space–time spectral element SBP-SAT scheme; Section 2.2 presents the adjoint formulation, employing a dual–consistent SBP-SAT discretization to compute the sensitivities; Section 2.3 presents the calculation of the sensitivity matrix.

**2.1. Space-time spectral element discretization of heat equation using SBP-SAT.** We employ SBP differentiation operators to discretize the spatial and temporal derivatives. Applying these SBP operators allows the use of high-order schemes and permits flexibility in the discretization type in each subdomain (e.g., DG, CG, FD, FV) [23, 24].

Let  $\{x_i\}_{i=0}^{N_x}$  denote the grid points on a given interval  $[a, b]$ . The one-dimensional SBP differentiation operator of degree  $r$ ,  $\bar{D}_x \in \mathbb{R}^{(N_x+1) \times (N_x+1)}$ , approximates the spatial derivative  $\partial/\partial x$ , and satisfies the following properties: it differentiates exactly monomials up to degree  $r$ ,

$$\bar{D}_x \mathbf{x}^s = s \mathbf{x}^{s-1}, \quad s = 0, 1, \dots, r, \quad \mathbf{x} = [x_0, \dots, x_{N_x}]^\top,$$

and it admits the factorization  $\bar{D}_x = \bar{P}_x^{-1} \bar{Q}_x$ , where  $\bar{P}_x$  is symmetric positive definite and  $\bar{Q}_x + \bar{Q}_x^\top = \bar{E}_x = \text{diag}(-1, 0, \dots, 0, 1)$ .

Next, we seek to construct space–time SBP differentiation operators together with compatible quadrature rule for the space–time integrals, in a way that preserves discrete integration-by-parts identity. To extend the one-dimensional SBP operator to space–time, we first construct a one-dimensional temporal SBP operator  $\bar{D}_t \approx \partial/\partial t$  of the form  $\bar{D}_t = \bar{P}_t^{-1} \bar{Q}_t$  on collocation nodes  $\{t_j\}_{j=0}^{N_t} \subset [0, T]$ . The space–time differentiation operators are then defined as tensor products [45].

$$\mathbf{P} := \bar{P}_t \otimes \bar{P}_x, \quad \mathbf{Q}_x := \bar{P}_t \otimes \bar{Q}_x, \quad \mathbf{Q}_t := \bar{Q}_t \otimes \bar{P}_x,$$

and then define

$$\mathbf{D}_x := \mathbf{P}^{-1} \mathbf{Q}_x = \mathbf{I}_t \otimes \bar{D}_x, \quad \mathbf{D}_t := \mathbf{P}^{-1} \mathbf{Q}_t = \bar{D}_t \otimes \mathbf{I}_x,$$

where  $\mathbf{I}_x$  and  $\mathbf{I}_t$  are identity matrices of size  $(N_x+1) \times (N_x+1)$  and  $(N_t+1) \times (N_t+1)$ , respectively. The symmetric positive definite weight (quadrature) matrix  $\mathbf{P}$  defines an inner product via  $\langle \mathbf{x}, \mathbf{y} \rangle_{\mathbf{P}} := \mathbf{x}^T \mathbf{P} \mathbf{y}$  for given vectors  $\mathbf{x} \in \mathbb{R}^N$  and  $\mathbf{y} \in \mathbb{R}^N$ , where  $N = (N_x+1)(N_t+1)$ . It also induces the discrete norm defined by  $\|\mathbf{x}\|_{\mathbf{P}}^2 = \mathbf{x}^T \mathbf{P} \mathbf{x}$ . For vectors  $\mathbf{u}$  and  $\mathbf{v}$  containing the values of continuous functions  $u(x, t)$  and  $v(x, t)$  at the grid points, respectively, one has

$$\mathbf{u}^T \mathbf{P} \mathbf{v} \approx \int_{\Omega} uv \, d\Omega, \quad \mathbf{u}^T \mathbf{Q}_x \mathbf{v} \approx \int_{\Omega} u \frac{\partial v}{\partial x} \, d\Omega,$$

where  $\Omega$  is the space–time domain.

We proceed to define restriction operators to extract the boundary values on the west (left), east (right), south (initial) and north (terminal) faces of each element:

$$\mathbf{R}_w = \mathbf{I}_t \otimes \mathbf{e}_w^\top, \quad \mathbf{R}_e = \mathbf{I}_t \otimes \mathbf{e}_e^\top, \quad \mathbf{R}_s = \mathbf{e}_s^\top \otimes \mathbf{I}_x, \quad \mathbf{R}_n = \mathbf{e}_n^\top \otimes \mathbf{I}_x,$$

where

$$\begin{aligned}\mathbf{e}_w &= [1, 0, \dots, 0]^T \in \mathbb{R}^{N_x}, & \mathbf{e}_e &= [0, \dots, 0, 1]^T \in \mathbb{R}^{N_x}, \\ \mathbf{e}_s &= [1, 0, \dots, 0]^T \in \mathbb{R}^{N_t}, & \mathbf{e}_n &= [0, \dots, 0, 1]^T \in \mathbb{R}^{N_t}.\end{aligned}$$

The surface operators in direction of  $x$  and  $t$  are given as

$$\mathbf{E}_x := \mathbf{R}_e^T \bar{\mathbf{P}}_t \mathbf{R}_e - \mathbf{R}_w^T \bar{\mathbf{P}}_t \mathbf{R}_w, \quad \mathbf{E}_t := \mathbf{R}_n^T \bar{\mathbf{P}}_x \mathbf{R}_n - \mathbf{R}_s^T \bar{\mathbf{P}}_x \mathbf{R}_s.$$

Notice that

$$\mathbf{u}^T \mathbf{E}_x \mathbf{v} \approx \int_{\Gamma_x} u v n_x d\Gamma, \quad \mathbf{u}^T \mathbf{E}_t \mathbf{v} \approx \int_{\Gamma_t} u v n_t d\Gamma,$$

where  $\Gamma_x$  and  $\Gamma_t$  denote the spatial and temporal parts of the boundary of the space-time domain  $\Omega$ , respectively.

With these space-time SBP operators in place, we can now state the discrete integration-by-parts property that is central to the SBP framework. Consider integration-by-parts in continuous form for spatial dimension  $x$ ,

$$\int_{\Omega} u \frac{\partial v}{\partial x} d\Omega + \int_{\Omega} v \frac{\partial u}{\partial x} d\Omega = \int_{\Gamma_x} u v n_x d\Gamma.$$

In discrete form we have the analogous property

$$\begin{aligned}\langle \mathbf{u}, \mathbf{D}_x \mathbf{v} \rangle_{\mathbf{P}} + \langle \mathbf{v}, \mathbf{D}_x \mathbf{u} \rangle_{\mathbf{P}} &= \mathbf{u}^T \mathbf{P} \mathbf{D}_x \mathbf{v} + \mathbf{v}^T \mathbf{P} (\mathbf{D}_x \mathbf{u}) \\ &= \mathbf{u}^T \mathbf{P} (\mathbf{P}^{-1} \mathbf{Q}_x) \mathbf{v} + \mathbf{u}^T (\mathbf{Q}_x^T \mathbf{P}^{-1}) \mathbf{P} \mathbf{v} \\ &= \mathbf{u}^T (\mathbf{Q}_x + \mathbf{Q}_x^T) \mathbf{v} = \mathbf{u}^T \mathbf{E}_x \mathbf{v}.\end{aligned}$$

By replicating integration-by-parts at the discrete level, SBP-SAT schemes enforce boundary conditions weakly, systematically creating energy-stable numerical methods in conjugate heat transfer problems [24, 23].

Spectral element methods based on Legendre-Gauss-Lobatto (LGL) nodes combine the geometric flexibility of finite element methods with the exponential convergence of spectral methods for smooth solutions. Their built-in SBP differentiation operators ensure provable energy stability, making them particularly well suited for CHT problems [46].

A space-time spectral element discretization for multi-domain CHT problems attains high-order in both space and time. Within the SBP-SAT framework, initial/terminal, boundary, and interface conditions are imposed weakly yet stably via SAT penalties, yielding a consistent scheme admitting a global energy estimate that mirrors the continuous energy estimate.

In the following, we construct a space-time SBP-SAT spectral element scheme for solving the primal problem. Suppose the given space-time domain  $\Omega$  is partitioned into  $K$  non-overlapping elements as illustrated in Figure 1,

$$\bar{\Omega} = \bigcup_{k=1}^K \bar{\Omega}_k = \bigcup_{k=1}^K [a_k, b_k] \times [0, T].$$

Let  $u : \bar{\Omega} \rightarrow \mathbb{R}$  denote the (continuous) solution of the heat equation and define  $u^{(k)} := u|_{\Omega_k}$  as its restriction to element  $\Omega_k$ . Assume the elements are coupled at

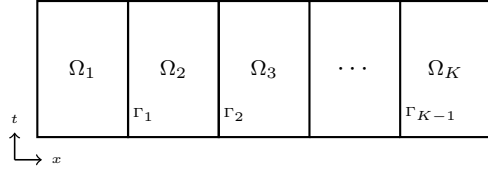


FIG. 1. Illustration of the partitioning of the space-time domain,  $\Omega$ , into non-overlapping elements,  $\Omega_k$ , with interfaces,  $\Gamma_k$ .

$\Gamma_k = \partial\Omega_k \cap \partial\Omega_{k+1}$  for  $1 \leq k \leq K-1$ , where continuity of the temperature and continuity of the normal heat flux are enforced:

$$(2.4) \quad \begin{aligned} u^{(k)} &= u^{(k+1)}, & \text{on } \Gamma_k, \\ \kappa^{(k)} u_x^{(k)} &= \kappa^{(k+1)} u_x^{(k+1)}, & \text{on } \Gamma_k. \end{aligned}$$

We assume the thermal diffusivity in each element is constant,  $\kappa^{(k)} = \kappa(\rho(\bar{x}))$  for some  $\bar{x} \in \Omega_k$  for  $1 \leq k \leq K$ . This ensures both energy conservation and the correct coupling at interface of elements.

To construct the SBP-SAT scheme, we assume  $\bar{D}_x$  and  $\bar{D}_t$  are pseudospectral differentiation matrices based on LGL collocation nodes at element  $k$ ,

$$\{x_i^{(k)}\}_{i=0}^{N_x} \subset [a_k, b_k], \quad \{t_j\}_{j=0}^{N_t} \subset [0, T].$$

Define

$$\begin{aligned} \mathbf{u}^{(k)} := & [u^{(k)}(x_0, t_0), u^{(k)}(x_1, t_0), \dots, u^{(k)}(x_{N_x}, t_0), \\ & \dots, u^{(k)}(x_0, t_{N_t}), u^{(k)}(x_1, t_{N_t}), \dots, u^{(k)}(x_{N_x}, t_{N_t})]^\top. \end{aligned}$$

Then the discretization of the heat equation using SBP-SAT scheme on element  $k$  leads to

$$(2.5) \quad (\mathbf{D}_t - \kappa^{(k)} \mathbf{D}_x^2) \mathbf{u}^{(k)} = \mathbf{f}^{(k)} - \mathbf{S}_w - \mathbf{S}_e - \mathbf{S}_0^{(k)} - \mathbf{S}_\Gamma^{(k, k-1)} - \mathbf{S}_\Gamma^{(k, k+1)},$$

where  $\mathbf{D}_x^2 = \mathbf{D}_x \mathbf{D}_x$  and  $\mathbf{f}^{(k)}$  contains the source data. The SAT terms  $\mathbf{S}_w$ ,  $\mathbf{S}_e$ ,  $\mathbf{S}_0^{(k)}$  and  $\mathbf{S}_\Gamma^{(k, k-1)}$  and  $\mathbf{S}_\Gamma^{(k, k+1)}$  are defined to enforce boundary, initial, and interface conditions in the following way. The coupling between subdomains using these SATs is illustrated in Figure 2.

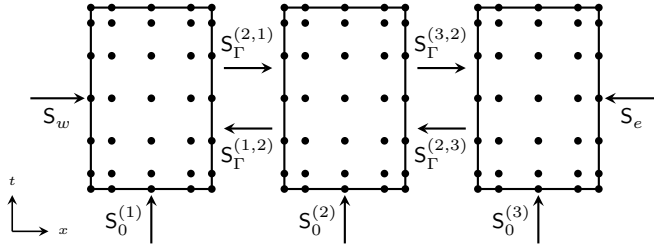


FIG. 2. Illustration of three subdomains discretized using LGL collocation nodes and coupled using boundary, initial, and interface SATs.

To enforce the boundary conditions on the left and right ends of the domain, we add  $S_w$  and  $S_e$  to the the first and last elements, respectively:

$$(2.6) \quad \begin{aligned} S_w &= \sigma_w P^{-1} R_w^T \bar{P}_t (R_w \mathbf{u}^{(1)} - R_w \mathbf{h}^{(1)}), \\ S_e &= \sigma_e P^{-1} R_e^T \bar{P}_t (R_e \mathbf{u}^{(K)} - R_e \mathbf{g}^{(K)}), \end{aligned}$$

where  $\mathbf{h}^{(1)}$  and  $\mathbf{g}^{(K)}$  contain the boundary functions  $h$  and  $g$  evaluated at grid points at the first and last elements, and  $\sigma_w$  and  $\sigma_e$  are positive penalty coefficients chosen to impose the boundary conditions weakly. These terms are set to be zero on all other elements. The SAT term for imposing the initial condition is defined as

$$(2.7) \quad S_0^{(k)} = \sigma_0 P^{-1} R_s^T \bar{P}_x (R_s \mathbf{u}^{(k)} - R_s \mathbf{q}^{(k)}), \quad 1 \leq k \leq K,$$

where  $\mathbf{q}^{(k)}$  contains the initial function  $q$  evaluated at grid points on element  $k$  and  $\sigma_0$  is a positive constant. The SAT terms for the interfaces are defined as

$$(2.8) \quad \begin{aligned} S_{\Gamma}^{(k,k-1)} &= \sigma_1 P^{-1} R_w^T \bar{P}_t (R_w \mathbf{u}^{(k)} - R_e \mathbf{u}^{(k-1)}) \\ &+ \sigma_2 P^{-1} R_w^T \bar{P}_t (\kappa^{(k)} R_w D_x \mathbf{u}^{(k)} - \kappa^{(k-1)} R_e D_x \mathbf{u}^{(k-1)}), \quad 2 \leq k \leq K, \\ &+ \tau_1 \kappa^{(k)} P^{-1} D_x^T R_w^T \bar{P}_t (R_w \mathbf{u}^{(k)} - R_e \mathbf{u}^{(k-1)}), \\ S_{\Gamma}^{(k,k+1)} &= \sigma_3 P^{-1} R_e^T \bar{P}_t (R_e \mathbf{u}^{(k)} - R_w \mathbf{u}^{(k+1)}) \\ &+ \sigma_4 P^{-1} R_e^T \bar{P}_t (\kappa^{(k)} R_e D_x \mathbf{u}^{(k)} - \kappa^{(k+1)} R_w D_x \mathbf{u}^{(k+1)}), \quad 1 \leq k \leq K-1, \\ &+ \tau_2 \kappa^{(k)} P^{-1} D_x^T R_e^T \bar{P}_t (R_e \mathbf{u}^{(k)} - R_w \mathbf{u}^{(k+1)}), \end{aligned}$$

where  $\sigma_1, \sigma_2, \sigma_3, \sigma_4, \tau_1$  and  $\tau_2$  are positive SAT coefficients. The discrete stability analysis leads to the following relation on SAT coefficients given in the following Theorem.

*Theorem 1.* Assume the SBP-SAT scheme given by (2.5)–(2.8) with zero source term. Let  $\hat{p}_0 = \mathbf{e}_w^T \bar{P}_x \mathbf{e}_w$  and  $\hat{p}_{N_x} = \mathbf{e}_e^T \bar{P}_x \mathbf{e}_e$ . Then under the conditions

$$(2.9) \quad \begin{aligned} \sigma_0 &> \frac{1}{2}, & \sigma_w &\geq \frac{\kappa_{\max}}{2\hat{p}_0}, & \sigma_e &\geq \frac{\kappa_{\max}}{2\hat{p}_{N_x}}, & \sigma_1 &= \sigma_3, \\ \sigma_2 &= s, & \sigma_4 &= 1+s, & \tau_1 &= -(1+s), & \tau_2 &= -s, & \forall s \in \mathbb{R}^+, \end{aligned}$$

the scheme is stable and following energy estimate holds:

$$(2.10) \quad \begin{aligned} \sum_{k=1}^K \|R_n \mathbf{u}^{(k)}\|_{\bar{P}_x}^2 &\leq \frac{1}{2\sigma_0 - 1} \sum_{k=1}^K \|R_s \mathbf{q}^{(k)}\|_{\bar{P}_x}^2 \\ &+ \sigma_w \|R_w \mathbf{h}^{(1)}\|_{\bar{P}_t}^2 + \sigma_e \|R_e \mathbf{g}^{(K)}\|_{\bar{P}_t}^2. \end{aligned}$$

*Proof.* The proof is given in Appendix (A).  $\square$

Notice that for primal stability, the SAT coefficients admit lower bounds determined by the mesh resolution, specifically the endpoint quadrature weights  $\hat{p}_0$  and  $\hat{p}_{N_x}$  of the one-dimensional SBP norm  $\bar{P}_x$ . These bounds also scale with the material properties through the maximal thermal diffusivity  $\kappa_{\max}$ .

To construct the global linear system, let

$$\hat{A}^{(k)} = P D_t - \kappa^{(k)} P D_x^2 + \sigma_0 R_s^T \bar{P}_x R_s, \quad \hat{\mathbf{f}}^{(k)} = P \mathbf{f}^{(k)} + \sigma_0 R_s^T \bar{P}_x R_s \mathbf{q}^{(k)},$$

where we have multiplied it by  $\mathsf{P}$  to avoid forming and applying  $\bar{\mathsf{P}}_x^{-1}$  and  $\bar{\mathsf{P}}_t^{-1}$  in the SAT terms, improving efficiency and numerical robustness. Then define

$$A^{(k)} = \begin{cases} \hat{A}^{(k)} + \sigma_w \mathsf{R}_w^\top \bar{\mathsf{P}}_t \mathsf{R}_w, & k = 1, \\ \hat{A}^{(k)} + \sigma_1 \mathsf{R}_w^\top \bar{\mathsf{P}}_t \mathsf{R}_w + \sigma_2 \kappa^{(k)} \mathsf{R}_w^\top \bar{\mathsf{P}}_t \mathsf{R}_w \mathsf{D}_x \\ \quad + \sigma_3 \mathsf{R}_e^\top \bar{\mathsf{P}}_t \mathsf{R}_e + \sigma_4 \kappa^{(k)} \mathsf{R}_e^\top \bar{\mathsf{P}}_t \mathsf{R}_e \mathsf{D}_x \\ \quad + \tau_1 \kappa^{(k)} \mathsf{D}_x^\top \mathsf{R}_w^\top \bar{\mathsf{P}}_t \mathsf{R}_w + \tau_2 \kappa^{(k)} \mathsf{D}_x^\top \mathsf{R}_e^\top \bar{\mathsf{P}}_t \mathsf{R}_e, & 2 \leq k \leq K-1, \\ \hat{A}^{(k)} + \sigma_e \mathsf{R}_e^\top \bar{\mathsf{P}}_t \mathsf{R}_e, & k = K, \end{cases}$$

and define

$$\mathbf{b}^{(k)} = \begin{cases} \hat{\mathbf{f}}^{(k)} + \sigma_w \mathsf{R}_w^\top \bar{\mathsf{P}}_t \mathsf{R}_w \mathbf{h}^{(k)}, & k = 1, \\ \hat{\mathbf{f}}^{(k)}, & 2 \leq k \leq K-1, \\ \hat{\mathbf{f}}^{(k)} + \sigma_e \mathsf{R}_e^\top \bar{\mathsf{P}}_t \mathsf{R}_e \mathbf{g}^{(k)}, & k = K. \end{cases}$$

Denote

$$\begin{aligned} B^{(k)} &= -\sigma_3 \mathsf{R}_e^\top \bar{\mathsf{P}}_t \mathsf{R}_w - \sigma_4 \kappa^{(k+1)} \mathsf{R}_e^\top \bar{\mathsf{P}}_t \mathsf{R}_w \mathsf{D}_x - \tau_2 \kappa^{(k)} \mathsf{D}_x^\top \mathsf{R}_e^\top \bar{\mathsf{P}}_t \mathsf{R}_w, \quad 1 \leq k \leq K-1, \\ C^{(k)} &= -\sigma_1 \mathsf{R}_w^\top \bar{\mathsf{P}}_t \mathsf{R}_e - \sigma_2 \kappa^{(k-1)} \mathsf{R}_w^\top \bar{\mathsf{P}}_t \mathsf{R}_e \mathsf{D}_x - \tau_1 \kappa^{(k)} \mathsf{D}_x^\top \mathsf{R}_w^\top \bar{\mathsf{P}}_t \mathsf{R}_e, \quad 2 \leq k \leq K. \end{aligned}$$

The global linear system is given by

$$\begin{bmatrix} A^{(1)} & B^{(1)} & 0 & \cdots & 0 \\ C^{(2)} & A^{(2)} & B^{(2)} & & \vdots \\ 0 & \ddots & \ddots & \ddots & 0 \\ \vdots & & C^{(K-1)} & A^{(K-1)} & B^{(K-1)} \\ 0 & \cdots & 0 & C^{(K)} & A^{(K)} \end{bmatrix} \begin{bmatrix} \mathbf{u}^{(1)} \\ \mathbf{u}^{(2)} \\ \vdots \\ \mathbf{u}^{(K)} \end{bmatrix} = \begin{bmatrix} \mathbf{b}^{(1)} \\ \mathbf{b}^{(2)} \\ \vdots \\ \mathbf{b}^{(K)} \end{bmatrix},$$

or in residual form by

$$(2.11) \quad \mathcal{R}(\mathbf{u}, \boldsymbol{\rho}) = \mathcal{A}(\boldsymbol{\rho})\mathbf{u} - \mathbf{b}.$$

Figure 3 shows the convergence of the space-time spectral element SBP-SAT method for a simple test example of the heat equation on the domain  $[-2, 1] \times [0, 1]$  with 10 elements, where we use the same number of collocation nodes in both temporal and spatial directions,  $N_t = N_x$ . The results are compared with a manufactured solution with homogeneous Dirichlet boundary conditions and an arbitrary heterogeneous given design  $\boldsymbol{\rho}$  on  $[0, 1]$ . The spectral convergence of the method is observed, with the error decreasing almost exponentially as the number of collocation nodes decreases and then remaining around  $10^{-14}$ , where floating-point round-off errors dominate. For the classical spectral element methods, spectral decay of the error is typically observed provided that the solution is a smooth function.

**2.2. Discrete dual consistent SBP-SAT scheme.** Let  $L$  be the given linear differential operator, heat equation with piecewise-constant (heterogeneous) diffusion coefficients, and let  $J(u)$  be a given functional. The adjoint problem solves  $L^*v = \mathcal{G} := \partial J/\partial u$  with the appropriate adjoint boundary and terminal data [47]. For example, it can be shown that when the primal PDE imposes its initial condition at  $t = 0$ , and

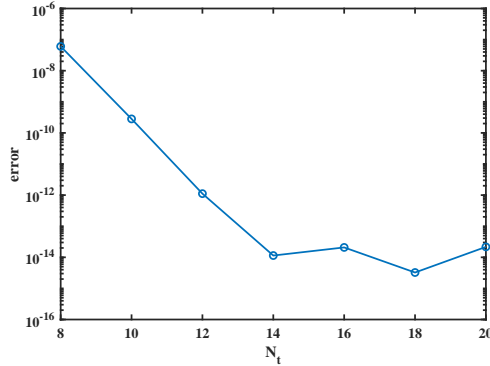


FIG. 3. *Convergence of the space-time spectral element SBP-SAT scheme for a simple test example of the heat equation.*

inhomogeneous Dirichlet boundary conditions, the adjoint PDE imposes a terminal condition at  $t = T$  and inhomogeneous Dirichlet boundary conditions for  $u$  become homogeneous Dirichlet boundary conditions for  $v$  at the same spatial nodes.

A discretization is *dual-consistent* (or *adjoint-consistent*) if it yields a discrete dual problem that is a consistent discretization of the dual PDE [36]. Let  $L_h$  and  $L_h^*$  be discrete operators approximating  $L$  and  $L^*$ , respectively, where  $h$  is the mesh resolution. The discretization is said to be dual (adjoint) consistent of order  $q \geq 1$  if

$$\|L_h^* \mathbf{v}_h - \mathbf{g}_h\|_{\mathbb{P}} = \mathcal{O}(h^q) \quad \text{as } h \rightarrow 0,$$

where  $\mathbf{v}_h$  and  $\mathbf{g}_h$  denote the projections of  $v$  and  $\mathcal{G}$  onto the discrete solution space.

In general, primal consistency of a discrete operator alone does not imply consistency of the dual solution, and optimal-order convergence of target functionals typically requires higher-order, dual-consistent discretizations. A functional estimate is called superconvergent, if the numerical solution satisfies  $\|\mathbf{u}_h - u(\mathbf{x}_h)\| = \mathcal{O}(h^r)$  but the functional  $J_h(\mathbf{u}_h)$  converges faster [37], e.g.,

$$|J_h(\mathbf{u}_h) - J(u(\mathbf{x}_h))| = \mathcal{O}(h^{r+s}) \quad \text{with } s > 0, \quad \text{as } h \rightarrow 0.$$

That is, the objective functional converges faster than the underlying solution approximation, the superconvergent method exhibits a higher rate of error reduction in the objective functional compared to the expected error for the overall approximation.

Dual-consistent PDE discretizations have been investigated in the literature [37, 38].

Hicken et al. [39] demonstrate that the superconvergent functional estimates can be derived using diagonal-norm SBP operators (i.e., SBP operators with diagonal weight matrices) from the dual consistency and stability of SBP-SAT discretizations, despite the reduced accuracy of the boundary stencils. Worku and Zingg in [40] extend this results to generalized SBP (GSBP) operators.

In our proposed scheme, time dual consistency is ensured if the primal PDE is stable and imposes the initial-time data via

$$\mathbf{S}_0^{(k)} = \sigma_0 \mathbb{P}^{-1} \mathbf{R}_s^T \bar{\mathbf{P}}_x (\mathbf{R}_s \mathbf{u}^{(k)} - \mathbf{R}_s \mathbf{q}^{(k)}), \quad 1 \leq k \leq K,$$

and the adjoint PDE imposes the terminal-time condition through

$$\mathbf{S}_f^{(k)} = \sigma_f \mathbb{P}^{-1} \mathbf{R}_n^T \bar{\mathbf{P}}_x (\mathbf{R}_n \mathbf{v}^{(k)} - \mathbf{0}), \quad 1 \leq k \leq K.$$

The adjoint of the associated matrix with respect to the SBP inner product is given by  $\mathcal{A}^\dagger = \mathbf{P}^{-1} \mathcal{A}^\top \mathbf{P}$ . Since  $\mathbf{P}$  is absorbed into the residual, we solve

$$\left( \frac{\partial \mathcal{R}}{\partial \mathbf{u}} \right)^\top \Lambda = \frac{\partial \mathbf{J}}{\partial \mathbf{u}} \quad \Rightarrow \quad \mathcal{A}^\top \Lambda = 2 \mathbf{P} \mathbf{u},$$

where  $\Lambda = [\boldsymbol{\lambda}^{(1)}; \dots; \boldsymbol{\lambda}^{(K)}]$  is the vector obtained by stacking the subdomain adjoint variables.

Under standard regularity, the resulting functional estimates are superconvergent. But with discontinuous coefficients (piecewise-constant diffusivity induced by  $\rho$ ), superconvergence behavior is retained only when interfaces are adequately resolved (e.g., via mesh refinement or by smoothing the design field with a filter [2]). A formal proof of superconvergent functional error for the proposed space–time spectral-element SBP-SAT scheme is left for future work.

**2.3. Calculating design sensitivity.** The design sensitivity is given by

$$\nabla_\rho \mathbf{J} = -\Lambda^\top \frac{\partial \mathcal{R}}{\partial \rho},$$

where

$$\nabla_\rho \mathbf{J} = \left[ \frac{\partial \mathbf{J}}{\partial \rho_1}; \frac{\partial \mathbf{J}}{\partial \rho_2}; \dots; \frac{\partial \mathbf{J}}{\partial \rho_K} \right].$$

In particular, for each component  $\rho_k$ ,

$$\frac{\partial \mathbf{J}}{\partial \rho_k} = - \sum_{j=1}^K \left( \frac{\partial \mathcal{R}_j}{\partial \rho_k} \right)^\top \boldsymbol{\lambda}^{(j)}, \quad 1 \leq k \leq K,$$

where  $\mathcal{R}_j$  denotes the  $j$ -th block row of  $\mathcal{R}$ . Notice that for the first element

$$\begin{aligned} \frac{\partial \mathcal{R}}{\partial \rho_1} &= \begin{bmatrix} \frac{\partial A^{(1)}}{\partial \rho_1} & \frac{\partial B^{(1)}}{\partial \rho_1} & 0 & \dots & 0 \\ \frac{\partial C^{(2)}}{\partial \rho_1} & \frac{\partial A^{(2)}}{\partial \rho_1} & \frac{\partial B^{(2)}}{\partial \rho_1} & \vdots & \vdots \\ 0 & \ddots & \ddots & \ddots & 0 \\ \vdots & \ddots & \frac{\partial C^{(K-1)}}{\partial \rho_1} & \frac{\partial A^{(K-1)}}{\partial \rho_1} & \frac{\partial B^{(K-1)}}{\partial \rho_1} \\ 0 & \dots & 0 & \frac{\partial C^{(K)}}{\partial \rho_1} & \frac{\partial A^{(K)}}{\partial \rho_1} \end{bmatrix} \begin{bmatrix} \mathbf{u}^{(1)} \\ \mathbf{u}^{(2)} \\ \vdots \\ \mathbf{u}^{(K)} \end{bmatrix} - \begin{bmatrix} \frac{\partial b^{(1)}}{\partial \rho_1} \\ \frac{\partial b^{(2)}}{\partial \rho_1} \\ \vdots \\ \frac{\partial b^{(K)}}{\partial \rho_1} \end{bmatrix} \\ &= \begin{bmatrix} \frac{\partial A^{(1)}}{\partial \rho_1} & \frac{\partial B^{(1)}}{\partial \rho_1} & \dots & 0 \\ \frac{\partial C^{(2)}}{\partial \rho_1} & 0 & \dots & \vdots \\ 0 & 0 & \dots & 0 \\ \vdots & \vdots & \ddots & \vdots \\ 0 & \dots & \dots & 0 \end{bmatrix} \begin{bmatrix} \mathbf{u}^{(1)} \\ \mathbf{u}^{(2)} \\ \vdots \\ \mathbf{u}^{(K)} \end{bmatrix}, \end{aligned}$$

then

$$\frac{\partial \mathbf{J}}{\partial \rho_1} = - \left( \begin{bmatrix} \frac{\partial A^{(1)}}{\partial \rho_1} & \frac{\partial B^{(1)}}{\partial \rho_1} \\ \frac{\partial C^{(2)}}{\partial \rho_1} & 0 \end{bmatrix} \begin{bmatrix} \mathbf{u}^{(1)} \\ \mathbf{u}^{(2)} \end{bmatrix} \right)^\top \cdot \begin{bmatrix} \boldsymbol{\lambda}^{(1)} \\ \boldsymbol{\lambda}^{(2)} \end{bmatrix},$$

since only the matrices for a given element depend on the design variable of that same element. Similarly for a given internal element

$$\frac{\partial J}{\partial \rho_k} = - \left( \begin{bmatrix} 0 & \frac{\partial B^{(k-1)}}{\partial \rho_k} & 0 \\ \frac{\partial C^{(k)}}{\partial \rho_k} & \frac{\partial A^{(k)}}{\partial \rho_k} & \frac{\partial B^{(k)}}{\partial \rho_k} \\ 0 & \frac{\partial C^{(k+1)}}{\partial \rho_k} & 0 \end{bmatrix} \begin{bmatrix} \mathbf{u}^{(k-1)} \\ \mathbf{u}^{(k)} \\ \mathbf{u}^{(k+1)} \end{bmatrix} \right)^T \cdot \begin{bmatrix} \boldsymbol{\lambda}^{(k-1)} \\ \boldsymbol{\lambda}^{(k)} \\ \boldsymbol{\lambda}^{(k+1)} \end{bmatrix}, \quad 2 \leq k \leq K-1,$$

and for the final element

$$\frac{\partial J}{\partial \rho_K} = - \left( \begin{bmatrix} 0 & \frac{\partial B^{(K-1)}}{\partial \rho_K} \\ \frac{\partial C^{(K)}}{\partial \rho_K} & \frac{\partial A^{(K)}}{\partial \rho_K} \end{bmatrix} \begin{bmatrix} \mathbf{u}^{(K-1)} \\ \mathbf{u}^{(K)} \end{bmatrix} \right)^T \cdot \begin{bmatrix} \boldsymbol{\lambda}^{(K-1)} \\ \boldsymbol{\lambda}^{(K)} \end{bmatrix}.$$

**3. Computational performance.** In the following we present numerical results to evaluate the performance and effectiveness of the proposed method. In Section 3.1, we provide numerical experiments that validate the optimal designs through comparisons with the independently computed reference solution. In Section 3.2, we report time-to-solution(wall-clock time) and provide cost-of-accuracy (memory requirement) curves by plotting the relative change in objective error versus runtime. All experiments were run in MATLAB R2024b on a Windows 11 laptop with an AMD Ryzen 7 8840U with 8 cores at 3.30 GHz and 32 GB of RAM.

**3.1. Verifying the optimal design in the numerical solver.** We consider a simplified model topology optimization problem subject to transient heat equation given by

$$(3.1) \quad \begin{aligned} u_t - (\kappa(x)u_x)_x &= f, & (x, t) \in [0, 1] \times [0, T], \\ u(0, t) &= 0, & u(1, t) = u_R, \\ u(x, 0) &= u_0(x), \end{aligned}$$

where  $u_R$  and  $f$  are given positive constants. Suppose there is an interface at  $\xi \in (0, 1)$  and  $\kappa(x)$  is a piecewise positive function given by,

$$\kappa(x) = \begin{cases} \kappa_1, & 0 \leq x \leq \xi, \\ \kappa_2, & \xi < x \leq 1, \end{cases} \quad \kappa_1, \kappa_2 > 0,$$

rendering the problem with just two design variables. The interface conditions at  $x = \xi$  are given by

$$u(\xi^-, t) = u(\xi^+, t), \quad \kappa_1 u_x(\xi^-, t) = \kappa_2 u_x(\xi^+, t).$$

A manufactured solution consistent with this design is derived in Appendix B, from which we obtain the initial condition  $u(x, 0) = u_0(x)$ .

We consider the objective functional given by

$$J(u) = \int_0^T \int_0^1 u(x, t)^2 dx dt,$$

and constrain the material by  $\kappa_1 + \kappa_2 = 0.75$ . Assume that  $\xi = 0.5$  so that the domain is split into two equal-length subdomains. Then the optimization problem

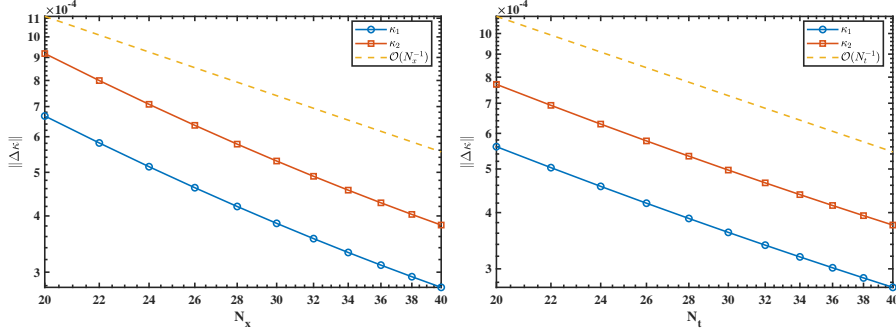


FIG. 4. Relative error of the **MMAHeat** optimal design (using **MMSHeat** as the reference). Left: spatial refinement by increasing  $N_x$  with  $N_t = 30$ ; right: temporal refinement by increasing  $N_t$  with  $N_x = 40$ .

is reduced to the one-dimensional search for  $\kappa_2 = 0.75 - \kappa_1$ , which is solved by the MATLAB-function `fminbnd` with a tolerance  $10^{-8}$ , yielding an approximate analytical minimizer

$$\kappa_1 = 0.4341, \quad \kappa_2 = 0.3158,$$

where the optimal value for the cost function is  $J = 5.1730$ . We refer to the corresponding solver as **MMAHeat**. The optimal allocation  $\kappa_1 > \kappa_2$  is physically intuitive: lowering the space-time  $L^2$ -temperature requires evacuating heat toward the cold boundary at  $x = 0$ .

To make a comparison with this (approximate) analytical solution, we run the topology optimization solver (which we denote by **MMAHeat**) with the same settings. MMA iterations were terminated when the maximum change in the design variables between successive iterates fell below  $10^{-8}$ , or after at most 100 iterations. To match the design variables with the  $\kappa_1$  and  $\kappa_2$  in analytical solution study, we remove the penalization effects in (2.1), setting  $p = 1$  (linear material interpolation),  $\kappa_{\max} = 1$  and  $\kappa_{\min} = 0$ . We enforce the same material budget used in the analytical solution by choosing  $V^* = 0.375$  in the volume constraint inequality (2.2) since it represents the mean-conductivity (due to being weighed by the element volume); on two equal elements this is equivalent to  $\kappa_1 + \kappa_2 = 0.75$ .

Figure 4 reports the relative error of the **MMAHeat** optimal design, using **MMSHeat** as the reference (treated as exact in this test). The error decreases steadily under mesh refinement in one direction, while the other direction is held fixed. The observed linear convergence is due to comparing two numerical results from two optimization algorithms that they are converging linearly.

Figure 5 demonstrates that the relative error in the optimal objective functional decreases as the mesh is refined in one direction (with the other held fixed). Together with Figure 4, this numerical experiment shows linear convergence of the discrete optimal design under mesh refinement and a superconvergent (approximately third-order) decay of the error in the optimal objective functional.

**3.2. Computational time and accuracy.** We consider a model topology optimization problem subject to transient heat problem on  $[0, 1] \times [0, 1]$  with the source term  $f(t, x) = 2 + \sin(10(x + t)) + \sin(10t)$ , zero Dirichlet boundary condition at  $x = 0$ , zero Neumann boundary condition at  $x = 1$  and zero initial condition given in

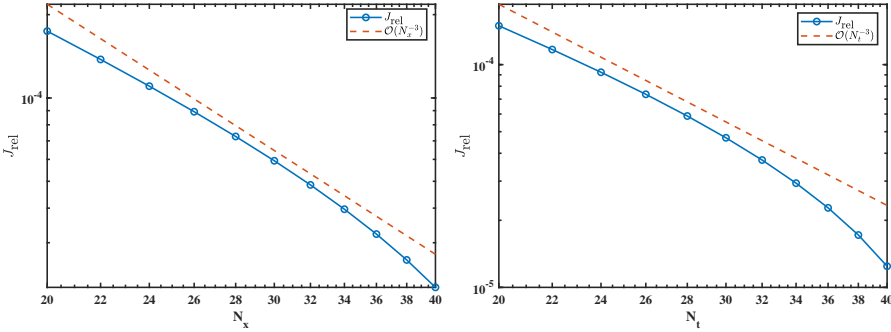


FIG. 5. Relative error of the optimal objective value (using *MMSHeat* as the reference). Left: versus spatial resolution  $N_x$  per element with  $N_t = 30$ ; right: versus temporal resolution  $N_t$  with  $N_x = 40$ .

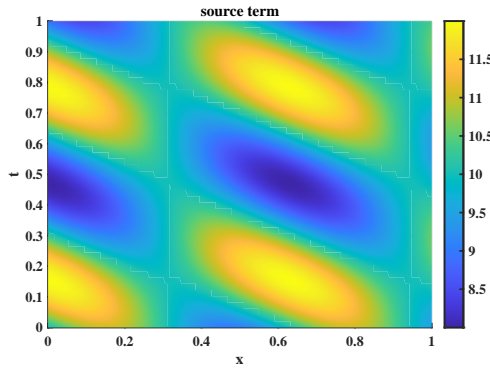


FIG. 6. The source term  $f(x, t)$  used in the numerical experiments.

the following

$$(3.2) \quad \begin{aligned} u_t - (\kappa(x)u_x)_x &= 10 + \sin(10(x+t)) + \sin(10t), & (x, t) \in [0, 1] \times [0, 1], \\ u_x(0, t) &= 0, \quad u(1, t) = 0, \\ u(x, 0) &= 0, \end{aligned}$$

In Figure 6 we show the source term  $f(x, t)$  used in the numerical experiments.

We compare timing and convergence rate of three forward solvers:

- (i) BE-FE: backward Euler in time with linear finite element in space, solved with time stepping (sequential);
- (ii) BE-FE-AAO: backward Euler in time with linear finite element in space, solved as a single all-at-once linear system;
- (iii) ST-SE: the space-time spectral element formulation explained in Section 2.1.

All runs use  $K = 50$  spatial elements for both FE and SE discretizations. The FE discretization is based on linear shape functions, while the spectral element discretization uses  $N_x = 5$  nodes per element (degree-4 polynomial basis), this number of nodes in the spatial direction is chosen to improve accuracy while keeping the cost reasonable. In all runs,  $p = 3$  in the equation (2.1) and the volume bound in the constraint (2.2) is fixed at  $V^* = 0.5$ .

Topology optimization is performed with MMA, starting from the same initial

design for all schemes at all time resolution levels. MMA iterations stop when the maximum design update per step falls below  $10^{-4}$ . Let  $\rho^{(i)}$  and  $J^{(i)}$  denote the optimized design and objective obtained at temporal resolution level  $i$  ( $N_t^e$  for FE and  $N_t^c$  for SE), we record the design change,

$$\|\Delta\rho\| := \|\rho^{(i)} - \rho^{(i-1)}\|_\infty,$$

and the relative change of the objective,

$$J_{\text{rel}} := \frac{|J^{(i)} - J^{(i-1)}|}{\max(|J^{(i-1)}|, \varepsilon)},$$

with  $\varepsilon = 10^{-12}$ . We use two specified tolerances  $\tau_\rho$  for the design change and  $\tau_J$  for the relative objective change.

Table 1 reports the wall-clock time and  $\|\Delta\rho\|$  for each setting. Convergence is declared when  $\|\Delta\rho\|$  is below  $\tau_\rho = 10^{-4}$  for two consecutive sweeps. In this numerical experiment, BE-FE reaches the target tolerance fastest, followed by ST-SE and BE-FE-AAO. The smallest design change occurs at  $N_t^e = 16,384$  for BE-FE and BE-FE-AAO, and at  $N_t^c = 15$  for ST-SE. In a fair comparison between ST-SE and BE-FE-AAO, we deduce that ST-SE attains the desired tolerance with the fewest DoFs in time (accuracy-cost in terms of memory) and the shortest wall-clock time (time-to-solution).

It is seen in this table that there is a jump in the value of  $\|\Delta\rho\|$  for the BE-FE (and BE-FE-AAO) method at around  $N_t^e = 64$ . This could be due to the fact that the optimizer becomes attracted to a different local minimum due to perturbations in the discretized objective function as the number of time steps is increased. Topology optimization problems are, in general, highly multi-modal and non-convex, meaning that it is not surprising that the optimizer can become attracted to a different local minimum when small perturbations are applied.

BE-FE			BE-FE-AAO			ST-SE		
$N_t^e$	time [s]	$\ \Delta\rho\ $	$N_t^e$	time [s]	$\ \Delta\rho\ $	$N_t^c$	time [s]	$\ \Delta\rho\ $
8	0.0270	0.050151	8	0.1007	0.050151	11	2.2695	0.000338
16	0.0200	0.338284	16	0.1237	0.338284	13	2.4287	0.000025
32	0.0207	0.011547	32	0.1949	0.011547	15	2.4863	0.000001
64	0.0323	0.006566	64	0.3699	0.006566			
128	0.0496	0.003575	128	0.6206	0.003575			
256	0.0913	0.001871	256	1.4553	0.001871			
512	0.1743	0.000922	512	3.0582	0.000922			
1024	0.3207	0.000482	1024	6.8655	0.000482			
2048	0.5869	0.000243	2048	13.1422	0.000243			
4096	1.1202	0.000122	4096	30.0512	0.000122			
8192	2.3068	0.000061	8192	58.2616	0.000061			
16384	5.3922	0.000030	16384	117.009	0.000030			

TABLE 1

Timing and design change comparison among the three forward solvers. Left: BE-FE (Backward Euler in time with finite elements in space, varying the number of time steps  $N_t^e$ ); middle: BE-FE-AAO (all-at-once version of BE-FE with varying  $N_t^e$ ); right: ST-SE (space-time spectral elements with one time element, varying the number of temporal collocation nodes  $N_t^c$ ). For the finest discretizations shown, the forward linear system sizes are 51 for BE-FE (solved at each of  $N_t^e = 16,384$  time steps), 835,635 for BE-FE-AAO, and 714 for ST-SE.

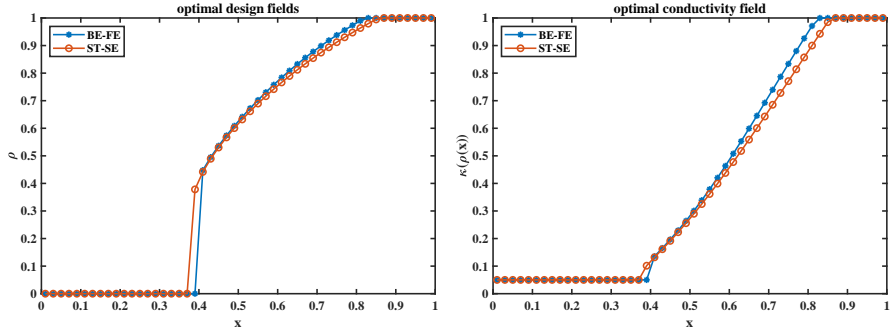


FIG. 7. Comparison of optimal designs and diffusivity fields from the BE-FE and ST-SE approaches.

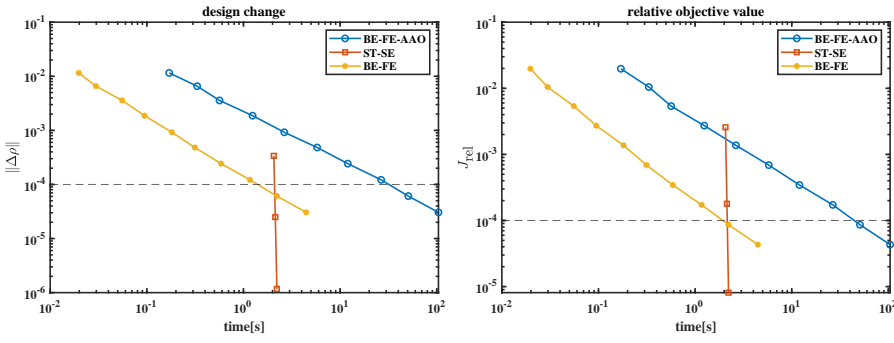


FIG. 8. Comparison of time from the three forward solvers (BE-FE, BE-FE-AAO and ST-SE) to reach the specified tolerance in the design change (left) and the relative change in objective (right). The size of the forward linear system in the finest mesh is 714 for ST-SE, 835, 635 for BE-FE-AAO, and 51 for BE-FE (solved at each of 16, 384 time steps).

Figure 7 shows the design field  $\rho$  and thermal diffusivity  $\kappa(\rho(x))$  at the finest resolution. Because the left boundary is insulated (zero Neumann boundary condition) while the right boundary is a cold sink (zero-temperature Dirichlet boundary condition), the optimal layout concentrates a single high-conductivity block next to the right boundary to channel heat out, with an almost linear tapering of the conductivity towards the low conductivity region furthest from the cold sink.

Figure 8 shows the time required by the three forward solvers BE-FE, ST-SE, and BE-FE-AAO, to reach the prescribed stopping tolerances for the design change. It can be seen that the fastest method is, in general, BE-FE, which is significantly faster than the all-at-once version BE-FE-AAO. This is as expected since the all-at-once represents much larger computational systems, which requires parallelization to make practical sense. Comparing the two all-at-once methods, BE-FE-AAO and ST-SE, it is seen that ST-SE provides significantly higher accuracy at a lower computational time. The ST-SE may become even more attractive when coupled with space-time parallelization. Notice that although the classical time-marching BE-FE scheme is faster for loose tolerances, it is inherently sequential and does not scale favorably to large-scale problems, and is therefore not a competitive option in this test.

Figure 9 demonstrates the evolution of the design change and the relative objective change over optimization iterations for BE-FE-AAO and ST-SE at the same number

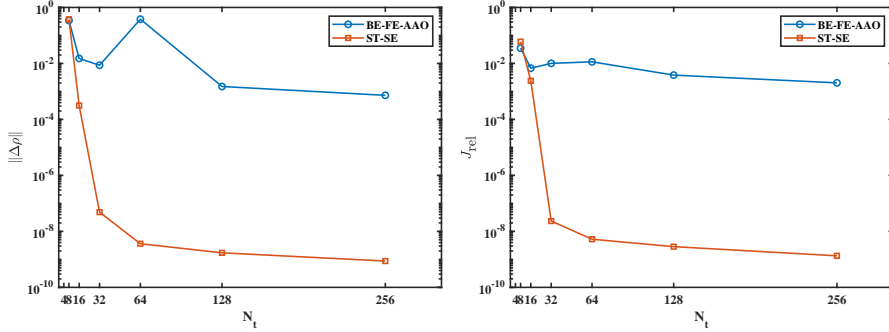


FIG. 9. Comparison of design change and relative change of the objective for two forward solvers BE-FE-AAO and ST-SE.

of node in temporal direction. The results demonstrate that the higher-order, dual consistent space-time scheme offer a significantly more favorable accuracy–cost trade-off. It is clearly seen that the BE-FE-AAO scheme is converging at an exceptionally slow rate when compared to the proposed ST-SE scheme.

**4. Concluding remarks.** We present a high-order space–time spectral element SBP–SAT framework for topology optimization of transient heat conduction. Interface and boundary conditions are imposed weakly via SATs, ensuring stability on heterogeneous subdomains. Using a discrete, dual-consistent space–time adjoint scheme, we compute design sensitivities over the full time horizon. Under standard smoothness assumptions, the resulting functional estimates exhibit superconvergent behavior. Numerical experiments produce optimal designs consistent with independently computed reference solutions. While the backward Euler time-stepping scheme shows faster convergence, it delivers lower accuracy and lacks parallel-in-time scaling. Compared with low-order backward Euler finite-element all-at-once solvers, our space–time scheme achieves superior time-to-solution and accuracy-per-cost. In particular, the proposed high-order space–time discretization attains higher resolution with fewer degrees of freedom, reducing computational time and memory while remaining stable. Large-scale performance further depends on effective linear solver technology. Some promising directions for future work include designing robust preconditioners for the coupled space–time linear systems and developing parallel-in-time strategies compatible with the monolithic space–time formulation.

## REFERENCES

- [1] M. P. Bendsøe, N. Kikuchi, Generating optimal topologies in structural design using a homogenization method, *Computer Methods in Applied Mechanics and Engineering* 71 (2) (1988) 197–224. doi:[https://doi.org/10.1016/0045-7825\(88\)90086-2](https://doi.org/10.1016/0045-7825(88)90086-2).
- [2] M. P. Bendsøe, O. Sigmund, *Topology Optimization: theory, methods, and applications*, 2nd Edition, Springer, Berlin Heidelberg, 2004. doi:[10.1007/978-3-662-05086-6](https://doi.org/10.1007/978-3-662-05086-6).
- [3] J. D. Deaton, R. V. Grandhi, A survey of structural and multidisciplinary continuum topology optimization: post 2000, *Struct. Multidiscip. Optim.* 49 (1) (2014) 1–38. doi:[10.1007/s00158-013-0956-z](https://doi.org/10.1007/s00158-013-0956-z).
- [4] J. Alexandersen, C. S. Andreasen, A review of topology optimisation for fluid-based problems, *Fluids* 5 (1) (2020). doi:[10.3390/fluids5010029](https://doi.org/10.3390/fluids5010029).
- [5] C. Zhuang, Z. Xiong, H. Ding, Topology optimization of the transient heat conduction problem on a triangular mesh, *Numerical Heat Transfer. Part B, Fundamentals* 64 (3) (2013) 239–262. doi:[10.1080/10407790.2013.791785](https://doi.org/10.1080/10407790.2013.791785).

- [6] C. Zhuang, Z. Xiong, A global heat compliance measure based topology optimization for the transient heat conduction problem, *Numerical Heat Transfer. Part B, Fundamentals* 65 (5) (2014) 445–471. doi:[10.1080/10407790.2013.873309](https://doi.org/10.1080/10407790.2013.873309).
- [7] T. Dbouk, A review about the engineering design of optimal heat transfer systems using topology optimization, *Applied Thermal Engineering* 112 (2017) 841–854. doi:<https://doi.org/10.1016/j.applthermaleng.2016.10.134>.
- [8] S. Wu, Y. Zhang, S. Liu, Topology optimization for minimizing the maximum temperature of transient heat conduction structure, *Structural and Multidisciplinary Optimization* 60 (2019) 69–82. doi:<https://doi.org/10.1007/s00158-019-02196-9>.
- [9] T. Zeng, H. Wang, M. Yang, J. AlexanderSEN, Topology optimization of heat sinks for instantaneous chip cooling using a transient pseudo-3d thermofluid model, *International Journal of Heat and Mass Transfer* 154 (2020). doi:[10.1016/j.ijheatmasstransfer.2020.119681](https://doi.org/10.1016/j.ijheatmasstransfer.2020.119681).
- [10] P. Michaleris, D. A. Tortorelli, C. A. Vidal, Tangent operators and design sensitivity formulations for transient non-linear coupled problems with applications to elastoplasticity, *International Journal for Numerical Methods in Engineering* 37 (14) (1994) 2471–2499. doi:[10.1002/nme.1620371408](https://doi.org/10.1002/nme.1620371408).
- [11] J. Dahl, J. S. Jensen, O. Sigmund, Topology optimization for transient wave propagation problems in one dimension, *Structural and Multidisciplinary Optimization* 36 (6) (2008) 585–595. doi:[10.1007/s00158-007-0192-5](https://doi.org/10.1007/s00158-007-0192-5).
- [12] M. J. B. Theulings, R. Maas, L. Noël, F. van Keulen, M. Langelaar, Reducing time and memory requirements in topology optimization of transient problems, *International Journal for Numerical Methods in Engineering* 125 (14) (2024) e7461. doi:[10.1002/nme.7461](https://doi.org/10.1002/nme.7461).
- [13] M. Appel, J. AlexanderSEN, One-shot parareal approach for topology optimization of transient heat flow, *SIAM Journal on Scientific Computing* 47 (6) (2025) B1450–B1480. doi:[10.1137/24M1696603](https://doi.org/10.1137/24M1696603).
- [14] A. S. I. Margetis, E. M. Papoutsis-Kiachagias, K. C. Giannakoglou, Reducing memory requirements of unsteady adjoint by synergistically using check-pointing and compression, *International Journal for Numerical Methods in Fluids* 95 (1) (2023) 23–43. doi:<https://doi.org/10.1002/fld.5136>.
- [15] K. Yaji, M. Ogino, C. Chen, K. Fujita, Large-scale topology optimization incorporating local-in-time adjoint-based method for unsteady thermal-fluid problem, *Structural and Multidisciplinary Optimization* 58 (2) (2018) 817–822. doi:[10.1007/s00158-018-1922-6](https://doi.org/10.1007/s00158-018-1922-6).
- [16] M. Appel, J. AlexanderSEN, Space-time multigrid methods suitable for topology optimisation of transient heat conduction, arXiv preprint arXiv:2505.10168 (2025).  
URL <https://arxiv.org/abs/2505.10168>
- [17] J. AlexanderSEN, M. Appel, Large-scale topology optimisation of time-dependent thermal conduction using space-time finite elements and a parallel space-time multigrid preconditioner, arXiv preprint arXiv:2508.09589 (2025).  
URL <https://arxiv.org/abs/2508.09589>
- [18] N. K. Yamaleev, B. Diskin, E. J. Nielsen, Local-in-time adjoint-based method for design optimization of unsteady flows, *Journal of Computational Physics* 229 (14) (2010) 5394–5407. doi:<https://doi.org/10.1016/j.jcp.2010.03.045>.
- [19] M. Zahr, P.-O. Persson, An adjoint method for a high-order discretization of deforming domain conservation laws for optimization of flow problems, *Journal of Computational Physics* 326 (2016) 516–543. doi:<https://doi.org/10.1016/j.jcp.2016.09.012>.
- [20] C. Saglietti, P. Schlatter, E. Wadbro, M. Berggren, D. S. Henningson, Topology optimization of heat sinks in a square differentially heated cavity, *International Journal of Heat and Fluid Flow* 74 (2018) 36–52. doi:[10.1016/j.ijheatfluidflow.2018.08.004](https://doi.org/10.1016/j.ijheatfluidflow.2018.08.004).
- [21] H. Nobis, P. Schlatter, E. Wadbro, M. Berggren, D. S. Henningson, Topology optimization of unsteady flows using the spectral element method, *Comput. & Fluids* 239 (2022) Paper No. 105387, 14. doi:[10.1016/j.compfluid.2022.105387](https://doi.org/10.1016/j.compfluid.2022.105387).
- [22] H. Nobis, P. Schlatter, E. Wadbro, M. Berggren, D. S. Henningson, Modal laminar-turbulent transition delay by means of topology optimization of superhydrophobic surfaces, *Comput. Methods Appl. Mech. Engrg.* 403 (2023) Paper No. 115721, 24. doi:[10.1016/j.cma.2022.115721](https://doi.org/10.1016/j.cma.2022.115721).
- [23] M. Svärd, J. Nordström, Review of summation-by-parts schemes for initial-boundary-value problems, *J. Comput. Phys.* 268 (2014) 17–38. doi:[10.1016/j.jcp.2014.02.031](https://doi.org/10.1016/j.jcp.2014.02.031).
- [24] D. C. Del Rey Fernández, J. E. Hicken, D. W. Zingg, Review of summation-by-parts operators with simultaneous approximation terms for the numerical solution of partial differential equations, *Comput. & Fluids* 95 (2014) 171–196. doi:[10.1016/j.compfluid.2014.02.016](https://doi.org/10.1016/j.compfluid.2014.02.016).
- [25] M. H. Carpenter, J. Nordström, D. Gottlieb, A stable and conservative interface treatment of arbitrary spatial accuracy, *J. Comput. Phys.* 148 (2) (1999) 341–365. doi:[10.1006/jcph.1998.6001](https://doi.org/10.1006/jcph.1998.6001).

1998.6114.

- [26] K. Mattsson, Boundary procedures for summation-by-parts operators, *J. Sci. Comput.* 18 (1) (2003) 133–153. doi:[10.1023/A:1020342429644](https://doi.org/10.1023/A:1020342429644).
- [27] J. Lindström, J. Nordström, A stable and high-order accurate conjugate heat transfer problem, *J. Comput. Phys.* 229 (14) (2010) 5440–5456. doi:[10.1016/j.jcp.2010.04.010](https://doi.org/10.1016/j.jcp.2010.04.010).
- [28] J. Nordström, J. Berg, Conjugate heat transfer for the unsteady compressible Navier-Stokes equations using a multi-block coupling, *Comput. & Fluids* 72 (2013) 20–29. doi:[10.1016/j.compfluid.2012.11.018](https://doi.org/10.1016/j.compfluid.2012.11.018).
- [29] T. Lundquist, A. Malan, J. Nordström, A hybrid framework for coupling arbitrary summation-by-parts schemes on general meshes, *J. Comput. Phys.* 362 (2018) 49–68. doi:[10.1016/j.jcp.2018.02.018](https://doi.org/10.1016/j.jcp.2018.02.018).
- [30] J. Nordström, T. Lundquist, Summation-by-parts in time, *J. Comput. Phys.* 251 (2013) 487–499. doi:[10.1016/j.jcp.2013.05.042](https://doi.org/10.1016/j.jcp.2013.05.042).
- [31] J. Nordström, T. Lundquist, Summation-by-parts in time: the second derivative, *SIAM J. Sci. Comput.* 38 (3) (2016) A1561–A1586. doi:[10.1137/15M103861X](https://doi.org/10.1137/15M103861X).
- [32] L. Friedrich, G. Schnücke, A. R. Winters, D. C. Del Rey Fernández, G. J. Gassner, M. H. Carpenter, Entropy stable space-time discontinuous Galerkin schemes with summation-by-parts property for hyperbolic conservation laws, *J. Sci. Comput.* 80 (1) (2019) 175–222. doi:[10.1007/s10915-019-00933-2](https://doi.org/10.1007/s10915-019-00933-2).
- [33] J. Berg, J. Nordström, Superconvergent functional output for time-dependent problems using finite differences on summation-by-parts form, *J. Comput. Phys.* 231 (20) (2012) 6846–6860. doi:[10.1016/j.jcp.2012.06.032](https://doi.org/10.1016/j.jcp.2012.06.032).
- [34] S. Nikkar, J. Nordström, A dual consistent summation-by-parts formulation for the linearized incompressible Navier-Stokes equations posed on deforming domains, *J. Comput. Phys.* 376 (2019) 322–338. doi:[10.1016/j.jcp.2018.09.006](https://doi.org/10.1016/j.jcp.2018.09.006).
- [35] D. N. Arnold, F. Brezzi, B. Cockburn, L. D. Marini, Unified analysis of discontinuous Galerkin methods for elliptic problems, *SIAM J. Numer. Anal.* 39 (5) (2001) 1749–1779. doi:[10.1137/S0036142901384162](https://doi.org/10.1137/S0036142901384162).
- [36] R. Hartmann, Adjoint consistency analysis of discontinuous Galerkin discretizations, *SIAM J. Numer. Anal.* 45 (6) (2007) 2671–2696. doi:[10.1137/060665117](https://doi.org/10.1137/060665117).
- [37] N. A. Pierce, M. B. Giles, Adjoint recovery of superconvergent functionals from PDE approximations, *SIAM Rev.* 42 (2) (2000) 247–264. doi:[10.1137/S0036144598349423](https://doi.org/10.1137/S0036144598349423).
- [38] M. B. Giles, E. Süli, Adjoint methods for PDEs: a posteriori error analysis and postprocessing by duality, *Acta Numer.* 11 (2002) 145–236. doi:[10.1017/S096249290200003X](https://doi.org/10.1017/S096249290200003X).
- [39] J. E. Hicken, D. W. Zingg, Superconvergent functional estimates from summation-by-parts finite-difference discretizations, *SIAM Journal on Scientific Computing* 33 (2) (2011) 893–922. doi:[10.1137/100790987](https://doi.org/10.1137/100790987).
- [40] Z. A. Worku, D. W. Zingg, Stability and functional superconvergence of narrow-stencil second-derivative generalized summation-by-parts discretizations, *J. Sci. Comput.* 90 (1) (2022) Paper No. 42, 32. doi:[10.1007/s10915-021-01707-5](https://doi.org/10.1007/s10915-021-01707-5).
- [41] O. Sigmund, K. Maute, Topology optimization approaches, *Struct. Multidiscip. Optim.* 48 (6) (2013) 1031–1055. doi:[10.1007/s00158-013-0978-6](https://doi.org/10.1007/s00158-013-0978-6).
- [42] M. B. Giles, N. A. Pierce, An introduction to the adjoint approach to design, *Flow, Turbulence and Combustion* 65 (3) (2000) 393–415. doi:[10.1023/A:1011430410075](https://doi.org/10.1023/A:1011430410075).
- [43] M. H. Carpenter, J. Nordström, D. Gotthieb, Revisiting and extending interface penalties for multi-domain summation-by-parts operators, *J. Sci. Comput.* 45 (1-3) (2010) 118–150. doi:[10.1007/s10915-009-9301-5](https://doi.org/10.1007/s10915-009-9301-5).
- [44] K. Svanberg, The method of moving asymptotes—a new method for structural optimization, *Internat. J. Numer. Methods Engrg.* 24 (2) (1987) 359–373. doi:[10.1002/nme.1620240207](https://doi.org/10.1002/nme.1620240207).
- [45] D. C. Del Rey Fernández, J. E. Hicken, D. W. Zingg, Simultaneous approximation terms for multi-dimensional summation-by-parts operators, *J. Sci. Comput.* 75 (1) (2018) 83–110. doi:[10.1007/s10915-017-0523-7](https://doi.org/10.1007/s10915-017-0523-7).
- [46] G. J. Gassner, A skew-symmetric discontinuous galerkin spectral element discretization and its relation to sbp-sat finite difference methods, *SIAM Journal on Scientific Computing* 35 (3) (2013) A1233–A1253. doi:[10.1137/120890144](https://doi.org/10.1137/120890144).
- [47] C. Lanczos, *Linear differential operators*, D. Van Nostrand Co., Ltd., London-Toronto-New York-Princeton, N.J., 1961.  
URL <https://pubs.siam.org/doi/book/10.1137/1.9781611971187>

**A. Discrete stability analysis of the space-time SBP-SAT scheme.** The following lemma is needed in the proof of the stability for the space-time SBP-SAT scheme.

*Lemma 2.* (Discrete trace inequality) For any grid vector  $\mathbf{z}$ ,

$$\|\mathbf{R}_w \mathbf{z}\|_{\bar{\mathbf{P}}_t}^2 \leq \frac{1}{\hat{p}_0} \|\mathbf{z}\|_{\mathbf{P}}^2, \quad \|\mathbf{R}_e \mathbf{z}\|_{\bar{\mathbf{P}}_t}^2 \leq \frac{1}{\hat{p}_{N_x}} \|\mathbf{z}\|_{\mathbf{P}}^2,$$

where  $\hat{p}_0 = \mathbf{e}_w^\top \bar{\mathbf{P}}_x \mathbf{e}_w$ , and  $\hat{p}_{N_x} = \mathbf{e}_e^\top \bar{\mathbf{P}}_x \mathbf{e}_e$ .

*Proof.* Let  $\bar{\mathbf{P}}_x = \text{diag}(\hat{p}_0, \dots, \hat{p}_{N_x})$  and  $\bar{\mathbf{P}}_t = \text{diag}(\hat{q}_0, \dots, \hat{q}_{N_t})$ , so  $\hat{p}_0 = \mathbf{e}_w^\top \bar{\mathbf{P}}_x \mathbf{e}_w \leq \mathbf{z}^\top \bar{\mathbf{P}}_x \mathbf{z}$  for all  $\mathbf{z} \in \mathbb{R}^{N_x}$  is  $c = \hat{p}_0$ , since if we assume  $\mathbf{z} = \alpha \mathbf{e}_w$ , then  $\mathbf{z}^\top \bar{\mathbf{P}}_x \mathbf{z} = \alpha^2 \mathbf{e}_w^\top \bar{\mathbf{P}}_x \mathbf{e}_w = \alpha^2 \hat{p}_0$ , and  $(\mathbf{e}_w^\top \mathbf{z})^2 = (\mathbf{e}_w^\top \alpha \mathbf{e}_w)(\mathbf{e}_w^\top \alpha \mathbf{e}_w) = \alpha^2$ . Then substituting into  $c(\mathbf{e}_w^\top \mathbf{z})^2 \leq \mathbf{z}^\top \bar{\mathbf{P}}_x \mathbf{z}$  yields  $c \alpha^2 \leq \hat{p}_0 \alpha^2$ , forcing  $c \leq \hat{p}_0$ , so the largest possible value is  $c = \hat{p}_0$ . Now,

$$\|\mathbf{R}_w \mathbf{z}\|_{\bar{\mathbf{P}}_t}^2 \leq \sum_{j=1}^{N_t} \hat{q}_j (\mathbf{R}_w \mathbf{z})_j^2 \leq \sum_{j=1}^{N_t} \hat{q}_j \sum_{i=1}^{N_x} \frac{\hat{p}_i}{\hat{p}_0} z_i^2 \leq \frac{1}{\hat{p}_0} \sum_{j=1}^{N_t \times N_x} \mathbf{P}_{jj} z_j^2 = \frac{1}{\hat{p}_0} \|\mathbf{z}\|_{\mathbf{P}}^2,$$

since  $\mathbf{P} = \bar{\mathbf{P}}_t \otimes \bar{\mathbf{P}}_x$ . The other inequality can be established in the same way.  $\square$

*Proof of Theorem 1.* To derive a discrete energy estimate for the space–time scheme, we left–multiply (2.5) on each subdomain by  $(\mathbf{u}^{(k)})^\top \mathbf{P}$  and then sum over  $k = 1, \dots, K$ .

(A.1)

$$\begin{aligned} & \sum_{k=1}^K \mathbf{u}^{(k)^\top} \mathbf{P} \mathbf{D}_t \mathbf{u}^{(k)} - \sum_{k=1}^K \kappa^{(k)} \mathbf{u}^{(k)^\top} \mathbf{P} \mathbf{D}_x^2 \mathbf{u}^{(k)} \\ &= - \sum_{k=1}^K \mathbf{u}^{(k)^\top} \mathbf{P} \mathbf{S}_0^{(k)} - \mathbf{u}^{(1)^\top} \mathbf{P} \mathbf{S}_w - \mathbf{u}^{(K)^\top} \mathbf{P} \mathbf{S}_e - \sum_{k=2}^K \mathbf{S}_\Gamma^{(k, k-1)} - \sum_{k=1}^{K-1} \mathbf{S}_\Gamma^{(k, k+1)}. \end{aligned}$$

By the SBP property,

(A.2)

$$\mathbf{u}^{(k)^\top} \mathbf{P} \mathbf{D}_t \mathbf{u}^{(k)} = \frac{1}{2} \mathbf{u}^{(k)^\top} \mathbf{E}_t \mathbf{u}^{(k)} = \frac{1}{2} (\mathbf{R}_n \mathbf{u}^{(k)})^\top \bar{\mathbf{P}}_x (\mathbf{R}_n \mathbf{u}^{(k)}) - \frac{1}{2} (\mathbf{R}_s \mathbf{u}^{(k)})^\top \bar{\mathbf{P}}_x (\mathbf{R}_s \mathbf{u}^{(k)}).$$

Moreover, since  $\mathbf{P} \mathbf{D}_x^2 = \mathbf{E}_x \mathbf{D}_x - \mathbf{D}_x^\top \mathbf{P} \mathbf{D}_x$ , we have

$$\begin{aligned} -\mathbf{u}^{(k)^\top} \mathbf{P} \mathbf{D}_x^2 \mathbf{u}^{(k)} &= -\mathbf{u}^{(k)^\top} \mathbf{E}_x \mathbf{D}_x \mathbf{u}^{(k)} + \mathbf{u}^{(k)^\top} \mathbf{D}_x^\top \mathbf{P} \mathbf{D}_x \mathbf{u}^{(k)} \\ &= (\mathbf{R}_w \mathbf{u}^{(k)})^\top \bar{\mathbf{P}}_t (\mathbf{R}_w \mathbf{D}_x \mathbf{u}^{(k)}) - (\mathbf{R}_e \mathbf{u}^{(k)})^\top \bar{\mathbf{P}}_t (\mathbf{R}_e \mathbf{D}_x \mathbf{u}^{(k)}) + (\mathbf{D}_x \mathbf{u}^{(k)})^\top \mathbf{P} (\mathbf{D}_x \mathbf{u}^{(k)}). \end{aligned} \blacksquare$$

Substituting this and (A.2) into (A.1) and taking sum over  $k$  yields

$$\begin{aligned} & \frac{1}{2} \sum_{k=1}^K (\mathbf{R}_n \mathbf{u}^{(k)})^\top \bar{\mathbf{P}}_x (\mathbf{R}_n \mathbf{u}^{(k)}) + \sum_{k=1}^K \kappa^{(k)} \mathbf{u}^{(k)^\top} \mathbf{D}_x^\top \mathbf{P} \mathbf{D}_x \mathbf{u}^{(k)} \\ &= \sum_{k=1}^K \kappa^{(k)} (\mathbf{R}_e \mathbf{u}^{(k)})^\top \bar{\mathbf{P}}_t (\mathbf{R}_e \mathbf{D}_x \mathbf{u}^{(k)}) - \sum_{k=1}^K \kappa^{(k)} (\mathbf{R}_w \mathbf{u}^{(k)})^\top \bar{\mathbf{P}}_t (\mathbf{R}_w \mathbf{D}_x \mathbf{u}^{(k)}) \\ &+ \frac{1}{2} \sum_{k=1}^K (\mathbf{R}_s \mathbf{u}^{(k)})^\top \bar{\mathbf{P}}_x (\mathbf{R}_s \mathbf{u}^{(k)}) - \mathbf{u}^{(1)^\top} \mathbf{P} \mathbf{S}_w - \mathbf{u}^{(K)^\top} \mathbf{P} \mathbf{S}_e \\ &- \sum_{k=1}^K \mathbf{u}^{(k)^\top} \mathbf{P} \mathbf{S}_0^{(k)} - \sum_{k=2}^K \mathbf{u}^{(k)^\top} \mathbf{P} \mathbf{S}_\Gamma^{(k, k-1)} - \sum_{k=1}^{K-1} \mathbf{u}^{(k)^\top} \mathbf{P} \mathbf{S}_\Gamma^{(k, k+1)}. \end{aligned} \quad (A.3)$$

It is straightforward to verify that

$$(A.4) \quad \begin{aligned} -\mathbf{u}^{(1)\top} \mathbf{P} \mathbf{S}_w &= -\sigma_w \|\mathbf{R}_w \mathbf{u}^{(1)} - \frac{1}{2} \mathbf{R}_w \mathbf{h}^{(1)}\|_{\bar{\mathbf{P}}_t}^2 + \frac{\sigma_w}{4} \|\mathbf{R}_w \mathbf{h}^{(1)}\|_{\bar{\mathbf{P}}_t}^2, \\ -\mathbf{u}^{(K)\top} \mathbf{P} \mathbf{S}_e &= -\sigma_e \|\mathbf{R}_e \mathbf{u}^{(K)} - \frac{1}{2} \mathbf{R}_e \mathbf{g}^{(K)}\|_{\bar{\mathbf{P}}_t}^2 + \frac{\sigma_e}{4} \|\mathbf{R}_e \mathbf{g}^{(K)}\|_{\bar{\mathbf{P}}_t}^2, \end{aligned}$$

and, for any  $1 \leq k \leq K$ ,

$$(A.5) \quad \begin{aligned} \frac{1}{2} (\mathbf{R}_s \mathbf{u}^{(k)})^\top \bar{\mathbf{P}}_x (\mathbf{R}_s \mathbf{u}^{(k)}) - \mathbf{u}^{(k)\top} \mathbf{P} \mathbf{S}_0 \\ = -\frac{2\sigma_0-1}{2} \|\mathbf{R}_s \mathbf{u}^{(k)} - \frac{1}{2} \mathbf{R}_s \mathbf{q}^{(k)}\|_{\bar{\mathbf{P}}_x}^2 + \frac{1}{2(2\sigma_0-1)} \|\mathbf{R}_s \mathbf{q}^{(k)}\|_{\bar{\mathbf{P}}_x}^2. \end{aligned}$$

Substituting (A.4) and (A.5) into (A.3) gives

$$(A.6) \quad \begin{aligned} &\frac{1}{2} \sum_{k=1}^K \|\mathbf{R}_n \mathbf{u}^{(k)}\|_{\bar{\mathbf{P}}_x}^2 + \sum_{k=1}^K \kappa^{(k)} \|\mathbf{D}_x \mathbf{u}^{(k)}\|_{\mathbf{P}}^2 \\ &= \sum_{k=1}^K \kappa^{(k)} (\mathbf{R}_e \mathbf{u}^{(k)})^\top \bar{\mathbf{P}}_t (\mathbf{R}_e \mathbf{D}_x \mathbf{u}^{(k)}) - \sum_{k=1}^K \kappa^{(k)} (\mathbf{R}_w \mathbf{u}^{(k)})^\top \bar{\mathbf{P}}_t (\mathbf{R}_w \mathbf{D}_x \mathbf{u}^{(k)}) \\ &\quad - \sigma_w \|\mathbf{R}_w \mathbf{u}^{(1)} - \frac{1}{2} \mathbf{R}_w \mathbf{h}^{(1)}\|_{\bar{\mathbf{P}}_t}^2 + \frac{\sigma_w}{4} \|\mathbf{R}_w \mathbf{h}^{(1)}\|_{\bar{\mathbf{P}}_t}^2 \\ &\quad - \sigma_e \|\mathbf{R}_e \mathbf{u}^{(K)} - \frac{1}{2} \mathbf{R}_e \mathbf{g}^{(K)}\|_{\bar{\mathbf{P}}_t}^2 + \frac{\sigma_e}{4} \|\mathbf{R}_e \mathbf{g}^{(K)}\|_{\bar{\mathbf{P}}_t}^2 \\ &\quad - \frac{2\sigma_0-1}{2} \|\mathbf{R}_s \mathbf{u}^{(k)} - \frac{1}{2} \mathbf{R}_s \mathbf{q}^{(k)}\|_{\bar{\mathbf{P}}_x}^2 + \frac{1}{2(2\sigma_0-1)} \sum_{k=1}^K \|\mathbf{R}_s \mathbf{q}^{(k)}\|_{\bar{\mathbf{P}}_x}^2 \\ &\quad - \sum_{k=2}^K \mathbf{u}^{(k)\top} \mathbf{P} \mathbf{S}_\Gamma^{(k, k-1)} - \sum_{k=1}^{K-1} \mathbf{u}^{(k)\top} \mathbf{P} \mathbf{S}_\Gamma^{(k, k+1)}. \end{aligned}$$

Then using Young's inequality, for any  $\alpha > 0$ ,

$$(A.7) \quad -\kappa^{(1)} (\mathbf{R}_w \mathbf{u}^{(1)})^\top \bar{\mathbf{P}}_t (\mathbf{R}_w \mathbf{D}_x \mathbf{u}^{(1)}) \leq \frac{\alpha \kappa^{(1)}}{2} \|\mathbf{R}_w \mathbf{u}^{(1)}\|_{\bar{\mathbf{P}}_t}^2 + \frac{\kappa^{(1)}}{2\alpha} \|\mathbf{R}_w \mathbf{D}_x \mathbf{u}^{(1)}\|_{\bar{\mathbf{P}}_t}^2$$

Notice that by using Lemma (2)

$$(A.8) \quad \|\mathbf{R}_w \mathbf{D}_x \mathbf{u}^{(1)}\|_{\bar{\mathbf{P}}_t}^2 \leq \frac{1}{\hat{p}_0} \|\mathbf{D}_x \mathbf{u}^{(1)}\|_{\mathbf{P}}^2,$$

also

$$(A.9) \quad \|\mathbf{R}_w \mathbf{u}^{(1)}\|_{\bar{\mathbf{P}}_t}^2 \leq 2 \|\mathbf{R}_w \mathbf{u}^{(k)} - \frac{1}{2} \mathbf{R}_w \mathbf{h}^{(1)}\|_{\bar{\mathbf{P}}_t}^2 + \frac{1}{2} \|\mathbf{R}_w \mathbf{h}^{(1)}\|_{\bar{\mathbf{P}}_t}^2.$$

Then we choose  $\alpha = \sigma_w / \kappa^{(1)}$  and substitute this and (A.8) in (A.7) to obtain

$$(A.10) \quad \begin{aligned} -\kappa^{(1)} (\mathbf{R}_w \mathbf{u}^{(1)})^\top \bar{\mathbf{P}}_t (\mathbf{R}_w \mathbf{D}_x \mathbf{u}^{(1)}) &\leq \sigma_w \|\mathbf{R}_w \mathbf{u}^{(k)} - \frac{1}{2} \mathbf{R}_w \mathbf{h}^{(1)}\|_{\bar{\mathbf{P}}_t}^2 \\ &\quad + \frac{\sigma_w}{4} \|\mathbf{R}_w \mathbf{h}^{(1)}\|_{\bar{\mathbf{P}}_t}^2 + \frac{\kappa^{(1)}{}^2}{2\sigma_w \hat{p}_0} \|\mathbf{D}_x \mathbf{u}^{(1)}\|_{\mathbf{P}}^2. \end{aligned}$$

Doing the same for  $\kappa^{(K)} (\mathbf{R}_e \mathbf{u}^{(K)})^\top \bar{\mathbf{P}}_t (\mathbf{R}_e \mathbf{D}_x \mathbf{u}^{(K)})$  and substitute the result and (A.10)

in (A.6) to obtain for

$$\begin{aligned}
& \frac{1}{2} \sum_{k=1}^K \|\mathbf{R}_n \mathbf{u}^{(k)}\|_{\mathbf{P}_x}^2 + \sum_{k=2}^{K-1} \kappa^{(k)} \|\mathbf{D}_x \mathbf{u}^{(k)}\|_{\mathbf{P}}^2 \\
& + \kappa^{(1)} \left(1 - \frac{\kappa^{(1)}}{2\sigma_w \hat{p}_0}\right) \|\mathbf{D}_x \mathbf{u}^{(1)}\|_{\mathbf{P}}^2 + \kappa^{(K)} \left(1 - \frac{\kappa^{(K)}}{2\sigma_e \hat{p}_{N_x}}\right) \|\mathbf{D}_x \mathbf{u}^{(K)}\|_{\mathbf{P}}^2 \\
(A.11) \quad & \leq \sum_{k=2}^K \kappa^{(k)} (\mathbf{R}_e \mathbf{u}^{(k)})^\top \bar{\mathbf{P}}_t (\mathbf{R}_e \mathbf{D}_x \mathbf{u}^{(k)}) - \sum_{k=2}^K \kappa^{(k)} (\mathbf{R}_w \mathbf{u}^{(k)})^\top \bar{\mathbf{P}}_t (\mathbf{R}_w \mathbf{D}_x \mathbf{u}^{(k)}) \\
& + \frac{\sigma_w}{2} \|\mathbf{R}_w \mathbf{h}^{(1)}\|_{\bar{\mathbf{P}}_t}^2 + \frac{\sigma_e}{2} \|\mathbf{R}_e \mathbf{g}^{(K)}\|_{\bar{\mathbf{P}}_t}^2 + \frac{1}{2(2\sigma_0 - 1)} \sum_{k=1}^K \|\mathbf{R}_s \mathbf{q}^{(k)}\|_{\bar{\mathbf{P}}_x}^2 \\
& - \sum_{k=2}^K \mathbf{u}^{(k)^\top} \mathbf{P} \mathbf{S}_{\Gamma}^{(k, k-1)} - \sum_{k=1}^{K-1} \mathbf{u}^{(k)^\top} \mathbf{P} \mathbf{S}_{\Gamma}^{(k, k+1)}.
\end{aligned}$$

So far we need to assume

$$(A.12) \quad \sigma_0 \geq \frac{1}{2}, \quad \sigma_w \geq \frac{\kappa_{\max}}{2\hat{p}_0}, \quad \sigma_e \geq \frac{\kappa_{\max}}{2\hat{p}_{N_x}},$$

since  $\kappa^{(1)}, \kappa^{(K)} \leq \kappa_{\max}$  by definition. It remains to show a stability estimate for SATs at the interface. To simplify calculation we introduce a vector

$$\mathbf{d}_k = [\mathbf{R}_e \mathbf{u}^{(k)}; \mathbf{R}_w \mathbf{u}^{(k+1)}; \mathbf{R}_e \mathbf{D}_x \mathbf{u}^{(k)}; \mathbf{R}_w \mathbf{D}_x \mathbf{u}^{(k+1)}].$$

Collecting all the interface terms at an interface  $\Gamma_k = \partial\Omega_k \cap \partial\Omega_{k+1}$ , result in

$$\begin{aligned}
& \sum_{k=2}^K \kappa^{(k)} (\mathbf{R}_e \mathbf{u}^{(k)})^\top \bar{\mathbf{P}}_t (\mathbf{R}_e \mathbf{D}_x \mathbf{u}^{(k)}) - \sum_{k=2}^K \kappa^{(k)} (\mathbf{R}_w \mathbf{u}^{(k)})^\top \bar{\mathbf{P}}_t (\mathbf{R}_w \mathbf{D}_x \mathbf{u}^{(k)}) \\
& - \sum_{k=2}^K \mathbf{u}^{(k)^\top} \mathbf{P} \mathbf{S}_{\Gamma}^{(k, k-1)} - \sum_{k=1}^{K-1} \mathbf{u}^{(k)^\top} \mathbf{P} \mathbf{S}_{\Gamma}^{(k, k+1)} = \mathbf{d}_k^\top (\mathbf{M}_k \otimes \bar{\mathbf{P}}_t) \mathbf{d}_k,
\end{aligned}$$

where

$$\mathbf{M}_k = \frac{1}{2} \begin{bmatrix} -2\sigma_3 & \sigma_1 + \sigma_3 & \kappa^{(k)}(-\sigma_4 - \tau_2 + 1) & \kappa^{(k+1)}(\sigma_4 + \tau_1) \\ \sigma_1 + \sigma_3 & -2\sigma_1 & \kappa^{(k)}(\sigma_2 + \tau_2) & \kappa^{(k+1)}(-\sigma_2 - \tau_1 - 1) \\ \kappa^{(k)}(-\sigma_4 - \tau_2 + 1) & \kappa^{(k)}(\sigma_2 + \tau_2) & 0 & 0 \\ \kappa^{(k+1)}(\sigma_4 + \tau_1) & \kappa^{(k+1)}(-\sigma_2 - \tau_1 - 1) & 0 & 0 \end{bmatrix}. \blacksquare$$

In order to have a stable scheme, we need to find conditions on SAT parameters such that  $\mathbf{M}_k$  is negative semi-definite. For that we need to cancel out every columns with zero diagonal entries. This leads to  $\sigma_4 = 1 + \sigma_2$ , resulting in a system of equations with a one-parameter family of solutions

$$(A.13) \quad \sigma_2 = s, \quad \sigma_4 = 1 + s, \quad \tau_1 = -(1 + s), \quad \tau_2 = -s, \quad \forall s \in \mathbb{R}^+.$$

Then  $\mathbf{M}_k$  reduces to

$$\mathbf{M}_k = \begin{bmatrix} -\sigma_3 & \frac{\sigma_1 + \sigma_3}{2} & 0 & 0 \\ \frac{\sigma_1 + \sigma_3}{2} & -\sigma_1 & 0 & 0 \\ 0 & 0 & 0 & 0 \\ 0 & 0 & 0 & 0 \end{bmatrix},$$

which has non-zero eigenvalues

$$\lambda_1 = -\sigma_3, \quad \lambda_2 = \frac{(\sigma_1 + \sigma_3)^2}{4\sigma_3} - \sigma_1.$$

Then  $\mathbf{M}_k \otimes \bar{\mathbf{P}}_t$  is negative semi-definite, all eigenvalues of  $\mathbf{M}_k$  are non-positive, leading to

$$(A.14) \quad \sigma_1 = \sigma_3.$$

Then if (A.12), (A.13) and (A.14) hold, we obtain the following estimate from (A.11) for the given scheme:

$$\begin{aligned} & \frac{1}{2} \sum_{k=1}^K \|\mathbf{R}_n \mathbf{u}^{(k)}\|_{\bar{\mathbf{P}}_x}^2 + \sum_{k=2}^{K-1} \kappa^{(k)} \|\mathbf{D}_x \mathbf{u}^{(k)}\|_{\mathbf{P}}^2 \\ & + \kappa^{(1)} \left(1 - \frac{\kappa^{(1)}}{2\sigma_w \hat{p}_0}\right) \|\mathbf{D}_x \mathbf{u}^{(1)}\|_{\mathbf{P}}^2 + \kappa^{(K)} \left(1 - \frac{\kappa^{(K)}}{2\sigma_e \hat{p}_{N_x}}\right) \|\mathbf{D}_x \mathbf{u}^{(K)}\|_{\mathbf{P}}^2 \\ & \leq \frac{1}{2(2\sigma_0 - 1)} \sum_{k=1}^K \|\mathbf{R}_s \mathbf{q}^{(k)}\|_{\bar{\mathbf{P}}_x}^2 + \frac{\sigma_w}{2} \|\mathbf{R}_w \mathbf{h}^{(1)}\|_{\bar{\mathbf{P}}_t}^2 + \frac{\sigma_e}{2} \|\mathbf{R}_e \mathbf{g}^{(K)}\|_{\bar{\mathbf{P}}_t}^2, \end{aligned}$$

or (2.10) for a simplified version.  $\square$

For simplicity we assume a zero source term  $\mathbf{f}^{(k)} \equiv 0$ ; the nonzero case follows by applying Young's inequality to  $(\mathbf{u}^{(k)})^\top \mathbf{P} \mathbf{f}^{(k)}$  and absorbing the resulting  $\|\mathbf{u}^{(k)}\|_{\mathbf{P}}^2$  term into the diffusion energy via a discrete Poincaré inequality.

**B. A two-subdomain manufactured solution for the heat equation with constant heat source.** We consider the 1D heat equation with a constant source term  $f \in \mathbb{R}$ ,

$$(B.1) \quad u_t = (\kappa(x) u)_x + f, \quad (x, t) \in [0, 1] \times [0, T],$$

and a material interface at  $x = \xi \in (0, 1)$ . The thermal diffusivity is piecewise constant,

$$\kappa(x) = \begin{cases} \kappa_1, & 0 \leq x \leq \xi, \\ \kappa_2, & \xi < x \leq 1, \end{cases} \quad \kappa_1, \kappa_2 > 0.$$

The Dirichlet boundary conditions are given as

$$u(0, t) = 0, \quad u(1, t) = u_R, \quad t \in [0, T],$$

where  $u_R$  a given constant. The standard interface conditions at  $x = \xi$  are given by

$$u(\xi^-, t) = u(\xi^+, t), \quad \kappa_1 u_x(\xi^-, t) = \kappa_2 u_x(\xi^+, t).$$

We seek a manufactured solution  $u(x, t)$  to (B.1) as a combination of a steady part  $u_s(x)$  and a decaying transient part  $v(x, t)$ :

$$u(x, t) = u_s(x) + v(x, t).$$

We choose  $u_s(x)$  to absorb the constant source term and enforce the Dirichlet boundary conditions, and  $v(x, t)$  to enforce time dependence while keeping the boundary values fixed. The initial condition then would be calculated by

$$u(x, 0) = u_0(x), \quad x \in [0, 1].$$

We calculate the steady part of the solution in following way. In each subdomain we solve  $\kappa_i u''_s + f = 0$  with interface and boundary conditions. A convenient choice is a piecewise quadratic:

$$u_s(x) = \begin{cases} -\frac{f}{2\kappa_1} x^2 + A_1 x, & 0 \leq x \leq \xi, \\ -\frac{f}{2\kappa_2} x^2 + A_2 x + B_2, & \xi \leq x \leq 1. \end{cases}$$

Imposing boundary and interface conditions gives the coefficients explicitly

$$(B.2) \quad A_1 = \frac{\kappa_2 u_R + \frac{f}{2} \left( 1 + \xi^2 \left( \frac{\kappa_2}{\kappa_1} - 1 \right) \right)}{\xi \kappa_2 + (1 - \xi) \kappa_1},$$

$$(B.3) \quad A_2 = \frac{\kappa_1}{\kappa_2} A_1, \quad B_2 = u_R + \frac{f}{2\kappa_2} - A_2.$$

By construction,  $\kappa_i u''_s + f = 0$  identically in each subdomain and all boundary and interface conditions hold.

Next we calculate the transient part of the solution. Set  $v(x, t) = e^{-\lambda t} w(x)$  with  $\lambda > 0$  to be determined. Then  $v_t = \kappa(x) v_{xx}$  if and only if

$$\kappa_i w''_i + \lambda w_i = 0 \quad \text{in each subdomain,}$$

with homogeneous Dirichlet conditions  $w(0) = w(1) = 0$ . One form that satisfies this is

$$(B.4) \quad \begin{aligned} w_1(x) &= \sin(\alpha_1 x), & 0 \leq x \leq \xi, \\ w_2(x) &= r \sin(\alpha_2(1 - x)), & \xi \leq x \leq 1, \end{aligned}$$

where  $\alpha_i = \sqrt{\lambda/\kappa_i}$  and  $r$  is chosen for temperature continuity:

$$r = \frac{\sin(\alpha_1 \xi)}{\sin(\alpha_2(1 - \xi))}.$$

the flux continuity at  $x = \xi$  reads  $\kappa_1 w'_1(\xi) = \kappa_2 w'_2(\xi)$ , producing the following condition for  $\lambda$ :

$$(B.5) \quad \sqrt{\kappa_1} \cot(\alpha_1 \xi) + \sqrt{\kappa_2} \cot(\alpha_2(1 - \xi)) = 0, \quad \alpha_i = \sqrt{\lambda/\kappa_i}.$$

Any positive root  $\lambda$  of (B.5) yields a valid decaying transient.

Combining steady solution  $u_s$  and transient correction gives the manufactured solution

$$(B.6) \quad u(x, t) = u_s(x) + e^{-\lambda t} w(x)$$

with  $u_s$  from (B.2)–(B.3),  $w$  given by (B.4), and  $\lambda$  solving (B.5).

To verify the solution, we plug in (B.6) in right hand side of (B.1) in each subdomain,

$$u_t - \kappa_i u_{xx} = (-\lambda e^{-\lambda t} w) - \kappa_i (u''_s + e^{-\lambda t} w'') = -\lambda e^{-\lambda t} w - \kappa_i \left( -\frac{f}{\kappa_i} - \frac{\lambda}{\kappa_i} e^{-\lambda t} w \right) = f.$$

Thus (B.1), Dirichlet boundary conditions and the interface conditions at  $x = \xi$  hold.